HybridSail

Hybrid Solar Sails for Active Debris Removal

Final Report

Authors: Lourens Visagie[(1)], Theodoros Theodorou[(1)]
Affiliation: [1]. Surrey Space Centre - University of Surrey

ACT Researchers: Leopold Summerer

Date: 27 June 2011

Contacts:

Vaios Lappas
Tel: +44 (0) 1483 873412
Fax: +44 (0) 1483 689503
e-mail: V.Lappas@surrey.ac.uk

Leopold Summerer (Technical Officer)
Tel: +31 (0)71 565 4192
Fax: +31 (0)71 565 8018
e-mail: act@esa.int

Available on the ACT website
http://www.esa.int/act

Ariadna ID: 10-6411b
Ariadna study type: Standard
Contract Number: 4000101448/10/NL/CBi

Abstract

The historical practice of abandoning spacecraft and upper stages at the end of mission life has resulted in a polluted environment in some earth orbits. The amount of objects orbiting the Earth poses a threat to safe operations in space. Studies have shown that in order to have a sustainable environment in low Earth orbit, commonly adopted mitigation guidelines should be followed (the Inter-Agency Space Debris Coordination Committee has proposed a set of debris mitigation guidelines and these have since been endorsed by the United Nations) as well as Active Debris Removal (ADR).

HybridSail is a proposed concept for a scalable de-orbiting spacecraft that makes use of a deployable drag sail membrane and deployable electrostatic tethers to accelerate orbital decay. The HybridSail concept consists of deployable sail and tethers, stowed into a nano-satellite package. The nano-satellite, deployed from a mothership or from a launch vehicle will home in towards the selected piece of space debris using a small thruster-propulsion firing and magnetic attitude control system to dock on the debris. The docking process relies on either a net that envelops the debris piece or a mechanical grabber that can grip the target object.

Once docked, the magnetic attitude control system on the HybridSail craft will de-tumble the debris object so that it is in a stable roll, pitch and yaw orientation. At this point the sail and tethers will deploy and the combined drag force and electrostatic tether force will proceed to de-orbit the joined satellites.

This report gives results on the de-orbiting capabilities of such a concept, together with an analysis of the effects that influence the de-orbit times. We also report on the conceptual design of the satellite and docking system and give results from attitude control simulations.

This study was performed within the ESA Ariadna scheme.

Contents

1 Background

1.1 Orbital debris

The historical practice of abandoning spacecraft and upper stages at the end of mission life has resulted in a polluted environment in low earth orbit. The amount of objects orbiting the Earth poses a threat to safe operations in space. A collision in space does not only destroy the colliding objects, but also creates a cloud of additional debris pieces that can further harm other intact satellites (as demonstrated by the collision between Russia's Cosmos 2251 and a commercial Iridium satellite in 2009). If additional debris is generated during such a break-up at higher altitudes, it is not naturally removed by drag and can cause the on-set of a cascading effect during which the particles would engage in chain reactions until they are ground to a limiting size. Altitudes with such a critical particle concentration are already suspected to exist near 800, 1000 and 1500 km [1]

The majority of debris objects occur in low Earth orbit (LEO), at altitudes below 2000km. The figures below shows the distribution of objects by orbit and object type, taken from the 2006 catalogue (this was prior to the Cosmos/Iridium collision).

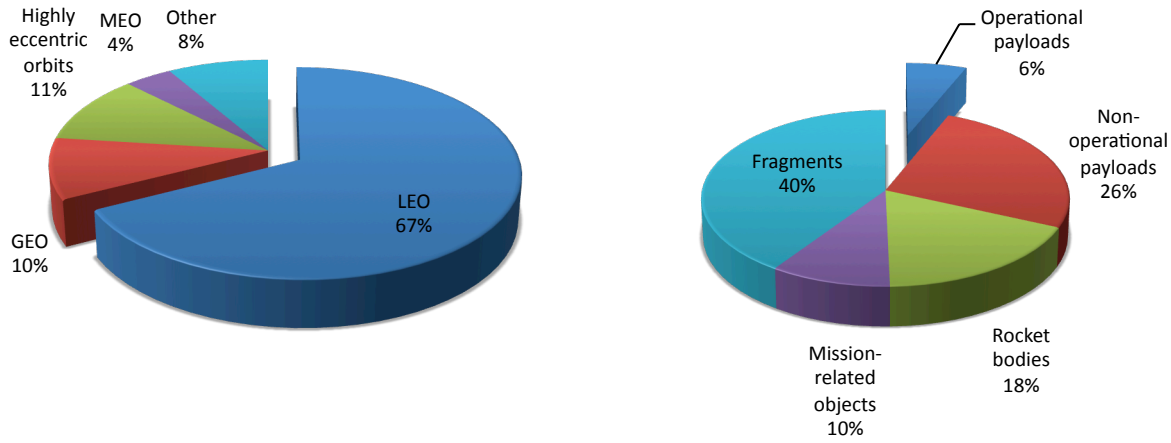

Figure 1 Distribution of Earth-orbiting objects by orbit type (left) and object type (right) [2]

It can be seen that only a small portion of the objects orbiting the Earth are operational, and that most objects are concentrated around LEO.

The trend is set to continue, as most of the planned launches for the current decade (2010 to 2019) are destined for LEO – 410 of the 1220 planned payloads will be launched to LEO. This number excludes rocket bodies, and satellites with a mass below 50kg.

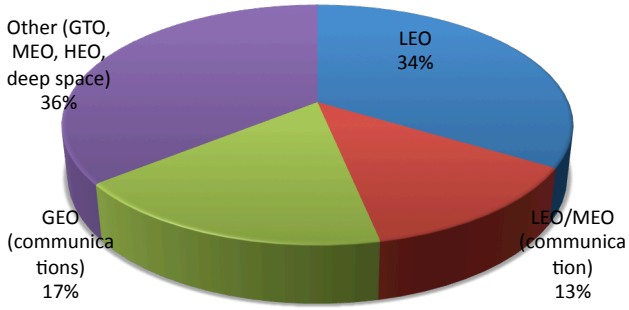

Figure 2 Satellites to be launched between 2010 and 2019 by orbit type [3]

The NASA orbital debris evolutionary model, LEGEND, predicts moderate linear increases in the MEO and GEO ranges, using a repetition of past launch cycles and assuming no post-mission disposal was carried out. But for LEO ranges there is a rapid non-linear increase in the orbital population as a result of new launches and collisions [4].

Their analysis has shown that 2 key strategies have to be implemented to stabilize the future LEO environment [5]:

1. A good implementation of the commonly-adopted mitigation measures
2. Active removal of existing debris at a rate of at least 5 significant objects per year

1.2 Mitigation Measures

The current accepted mitigation guidelines are based on the Inter-Agency Space Debris Coordination Committee (IADC) Space Debris Mitigation Guidelines [6]. The IADC is an international forum for the coordination of activities related to space debris and is comprised of the space agencies of 10 countries including ESA. In February 2007, the Scientific and Technical Subcommittee (STSC) of the United Nations' Committee on the Peaceful Uses of Outer Space (COPUOS) adopted a consensus set of space debris mitigation guidelines based on that of the IADC. The guidelines were accepted by the COPUOS and endorsed by the United Nations in January 2008. The guidelines relevant to LEO satellites and to this study can be summarized as [6]:

1. Limit debris released during normal operations
2. Minimise the potential for on-orbit break-up
    a. Minimise the potential for post mission break-ups resulting from stored energy
    b. Minimise the potential for break-ups during operational phase
3. Post mission disposal: A spacecraft or orbital stage should be left in an orbit in which atmospheric drag will limit the orbital lifetime after completion of operation. 25 years have been found to be a reasonable and appropriate limit.

1.3 Active Debris Removal (ADR)

Active Debris Removal is the action of identifying and disposing of existing orbital debris by moving it into a disposal orbit (one where atmospheric drag will limit the lifetime or a “graveyard” orbit where it will not interfere with other objects). The problem is quite complex because it requires either experimental contactless technologies, or complicated manoeuvring and docking operations, in addition to efficient propulsion with re-usability requirements.

Perhaps the easier part of ADR is the identification of priority pieces of debris. Some debris objects pose a greater collision risk than others. These objects are better candidates for ADR than others. The NASA LEGEND model suggests a selection criterion based on the product of the object mass and the collision probability, where the latter is a function of the object cross-section area and the object density of the orbit in which it occurs.

The US Space Surveillance Network (SSN) maintains a publicly available catalogue of tracked objects in Earth orbit. The information on each object is in the form of orbital elements (two-line element sets) that describes the orbit. Information was extracted from the catalogue (on 12 Dec 2010) to obtain the distribution plots below.

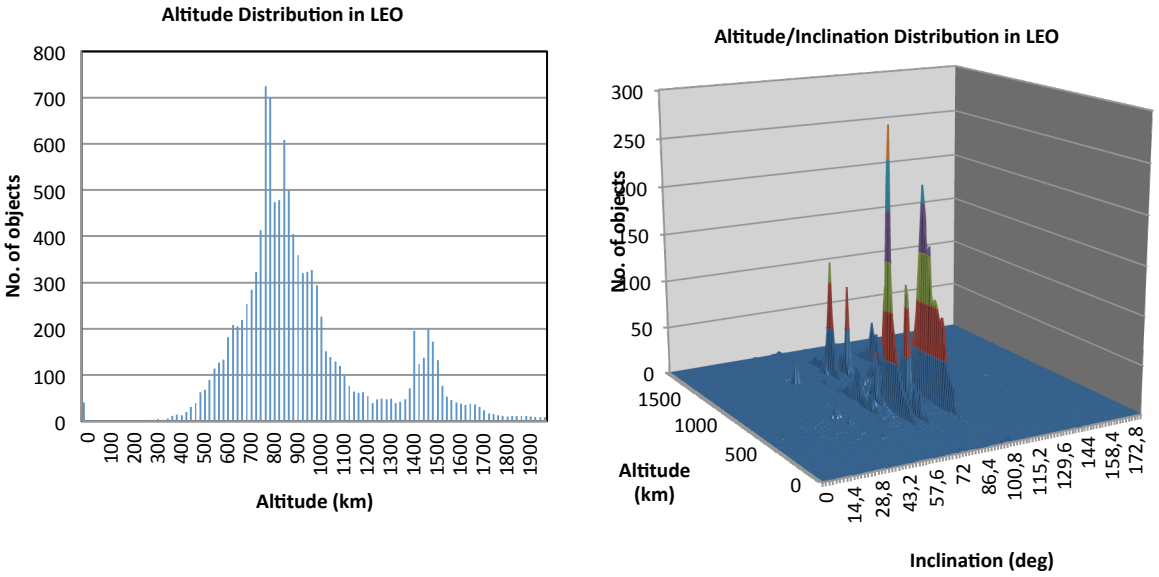

Figure 3 Distribution of objects in low Earth orbit

It can be seen that peak object densities occur around 800km and 1500km altitude, and also at 97.2° inclinations (at an altitude of 860 km) and 73.8° (720km).

Unfortunately the SSN catalogue does not contain information about the mass or cross-section area of objects, and no publicly available source exists for this information. Without the satellite mass and area knowledge, the best that the selection criterion can achieve is to identify objects in the higher density orbits.

For the purposes of this study, the ESA Advanced Concepts Team has provided a list of priority debris objects. All the objects in the list have perigee altitude above 700km, apogee altitude below 900km, eccentricity below 0.001 and mass exceeding 500kg.

Table 1-1 Priority list of debris objects for active debris removal

Average cross-section area (m^2)	Mass (kg)	Semi-major axis	Eccentricity	Inclination (deg)	Right-ascension of the ascending node (deg)	Argument of perigee (deg)
22.2521	661.05	7154.859	0.000249	86.4002	334.7577	72.5434
6.4859	1753.22	7158.468	0.0007	35.0457	93.339	188.8342
8.0062	693.76	7132.156	0.000872	35.0427	196.5135	326.2027

6.4859	1994.05	7120.482	0.000641	34.9942	105.1042	282.2124
3.7825	743.31	7089.467	0.000906	74.0129	142.1734	278.2267
1.7732	743.31	7102.456	0.000602	74.0374	305.1536	177.5348
12.9182	1421.21	7129.122	0.000881	74.0767	2.84	56.7027
5.8996	1486.62	7261.109	0.000933	81.2613	226.1147	289.782
-	508.42	7158.678	0.000939	98.5047	74.4704	161.1933
21.1594	2279.48	7129.309	0.000346	108.0085	183.1643	267.7558
1.7732	743.31	7158.929	0.000998	74.0455	122.2159	299.3001
12.9182	1421.21	7156.566	0.000471	74.0551	8.3423	358.0394
1.7732	743.31	7165.552	0.000995	74.0376	166.856	289.8727
3.5466	744.3	7175.16	0.000727	98.5979	82.246	309.454
7.0929	1923.69	7080.635	0.000341	98.1922	320.4069	136.1987
3.0905	629.34	7146.765	0.000212	108.0318	10.604	274.154
21.6139	2120.91	7221.955	0.000277	70.9998	192.1498	132.006
33.4262	8225.97	7217.136	0.000946	71.0023	167.7342	242.4867
3.0493	733.4	7265.165	0.000844	99.0179	212.3947	267.3074
-	3221.01	7228.007	0.000799	70.9218	338.4874	157.6445
33.4262	8225.97	7215.399	0.000349	71.0041	314.263	128.5404
-	3221.01	7222.68	0.000429	70.9958	211.4363	124.6571
12.9182	1421.21	7143.904	0.000576	74.0401	280.8718	250.4652
3.5466	815.66	7182.834	0.000649	98.9174	85.5927	10.4535
16.5395	2244.8	7256.73	0.00084	98.9994	256.6304	316.0426
-	3221.01	7229.364	0.000842	70.8729	213.2285	203.1169
33.4262	8225.97	7221.31	0.000627	71.0215	357.6447	283.2526
22.2825	1764.12	7139.285	0.000396	98.6952	228.2633	94.3321
2.1508	796.83	7193.017	9.09E-05	98.468	211.7472	85.0151
33.4262	8225.97	7220.64	5.09E-05	70.9649	12.445	73.0759
12.9182	1421.21	7160.037	0.000608	74.0281	136.4772	224.1406
19.2788	2493.56	7162.382	8.02E-05	98.5614	327.4721	80.7174
22.2825	1764.12	7148.4	0.000806	98.4919	201.9816	35.1036
13.1132	2724.48	7169.997	0.000145	98.58	259.3383	93.1622
2.2611	1337.96	7197.152	0.000134	98.3664	239.0998	84.8661
5.6413	891.97	7183.29	0.000277	98.5852	195.2318	234.6183
6.8852	1020.81	7229.833	0.001	98.8347	332.7928	11.0207
-	3221.01	7226.197	0.000792	71.0523	123.9866	24.8603
5.8424	970	7180.54	0.000137	98.6303	81.7095	60.1862
29.0095	5190	7080.652	0.000159	98.1991	327.2526	88.5102
33.4262	8225.97	7222.264	0.00049	70.996	70.2115	253.8401
-	3171.46	7229.619	0.000951	70.8338	188.2764	247.1589
25.8299	2730.43	7203.272	0.000151	98.6503	322.7285	56.6433
33.4262	8225.97	7218.69	0.000691	71.0088	195.6698	1.6454
12.9182	1421.21	7152.469	0.000455	74.0476	218.0031	101.4606
1.7732	743.31	7094.933	0.000337	73.9975	279.7907	222.186
3.5466	815.66	7220.218	0.000769	98.7481	344.313	119.0486
3.5466	815.66	7219.751	0.000905	98.6298	310.827	11.8542
20.4977	2468.78	7174.47	0.00019	98.4242	206.1816	49.156

21.6535	1764.12	7163.545	0.000237	98.2294	242.1384	229.9351
5.4363	2775.02	7189.291	0.000162	98.3049	266.8646	15.2104
13.2927	1969	7080.654	0.000094	98.2044	320.8825	52.078
14.9503	924	7177.173	0.000765	39.576	89.0772	42.5467
35.1642	9000	7224.091	0.000465	70.9958	221.5831	330.6496
2.2038	913.78	7197.61	0.000391	98.4454	214.3049	21.7428
10.8063	1450	7154.862	0.000513	98.1809	239.3917	162.9587
6.1981	1154	7216.518	0.00096	98.4725	335.7153	340.3165
6.8852	1060.46	7224.559	0.000949	98.8741	333.4819	359.7762
35.1642	9000	7223.626	0.00016	70.9774	180.7202	254.8075

2 Hybrid Solar Sail for Active Debris Removal

HybridSail is a concept that combines a large deployable reflective sail with embedded tethers and docking capability to yield a satellite that can be used to de-orbit debris pieces using a combination of aerodynamic drag, solar radiation pressure and electrostatic braking.

In drag-sail mode the deployed membranes will be used to increase the area of the spacecraft that will interact with the atmospheric particles, causing an increased drag and a faster de-orbiting. The size of the sail required to successfully de-orbit a satellite will depend on the mass of the spacecraft and its initial orbit.

The embedded tethers will operate on the principle of an electric sail [16]. The de-orbiting is accelerated by making use of momentum exchange with the ionospheric plasma stream. Electrostatic braking is a result of maintaining a negative charge in the tethers. The negative charge in the tether will deflect electrons in the ionosphere plasma, thereby exchanging momentum with it. The momentum loss in the satellite will result in a lower velocity and consequently a faster de-orbiting time.

The concept will build on an existing solar sail/drag sail project currently underway at the Surrey Space Centre, CubeSail, as well as the research carried out on plasma brake de-orbiting [16].

2.1 CubeSail

The objectives of the CubeSail project is to develop and flight test a deployable sail to demonstrate solar radiation pressure and drag de-orbiting. This project is a pathfinder mission that hopes to create options for de-orbiting of satellites and paves the way for solar sail propulsion.

The stowed satellite will have a CubeSat 3U form factor (10x10x34cm) and the square deployable sail has a size of 5m x 5m. The figure below shows this concept in its stowed configuration ready to be launched and in the deployed configuration.

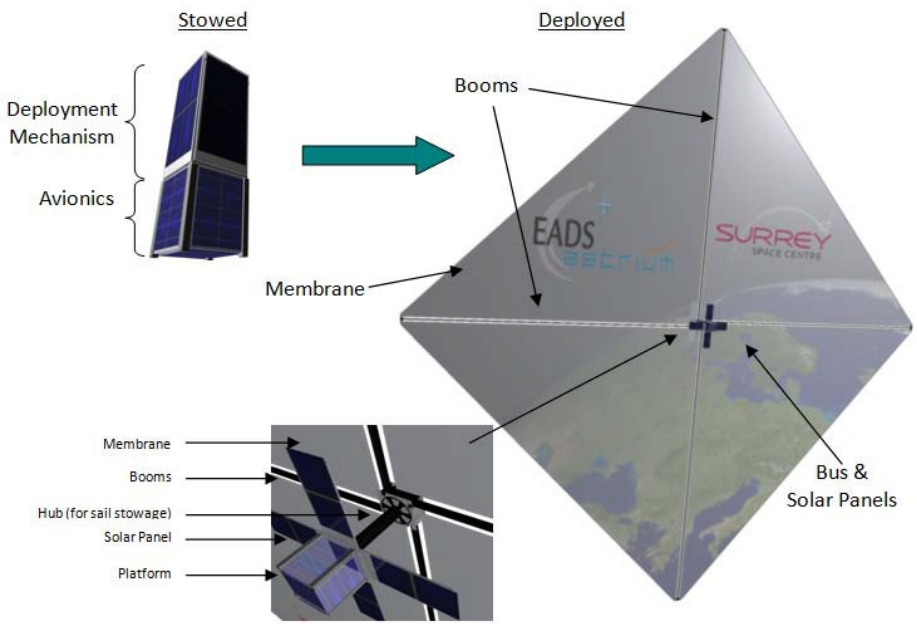

Figure 4 CubeSail stowed and deployed configurations

A scaled version of the deployment system has already been constructed at the Surrey Space Centre. This is a 1.7x1.7-meter breadboard model used to test different deployment configurations and folding patterns.

Figure 5 CubeSail 1.7m x 1.7m prototype

Launch of this spacecraft is planned for late 2011 and the project is funded by EADS/Astrium.

2.2 ADR using HybridSail

The HybridSail concept consists of deployable sail and tethers, stowed into a nano-satellite package. The nano-satellite, deployed from a mothership or from a launch vehicle will home in towards the selected piece of space debris. The nano-satellite will use a small thruster-propulsion firing and use its magnetic attitude control system to dock on the debris. The docking process relies on either a net that envelops the debris piece or a mechanical grabber that can grip the target object. The docking method is detailing in chapter 6.

Once docked, the magnetic attitude control system on the HybridSail craft will de-tumble the debris object so that it is in a stable roll, pitch and yaw orientation. At this point the sail and tethers will deploy and the combined drag force and electrostatic tether force will proceed to de-orbit the joined debris object-HybridSail.

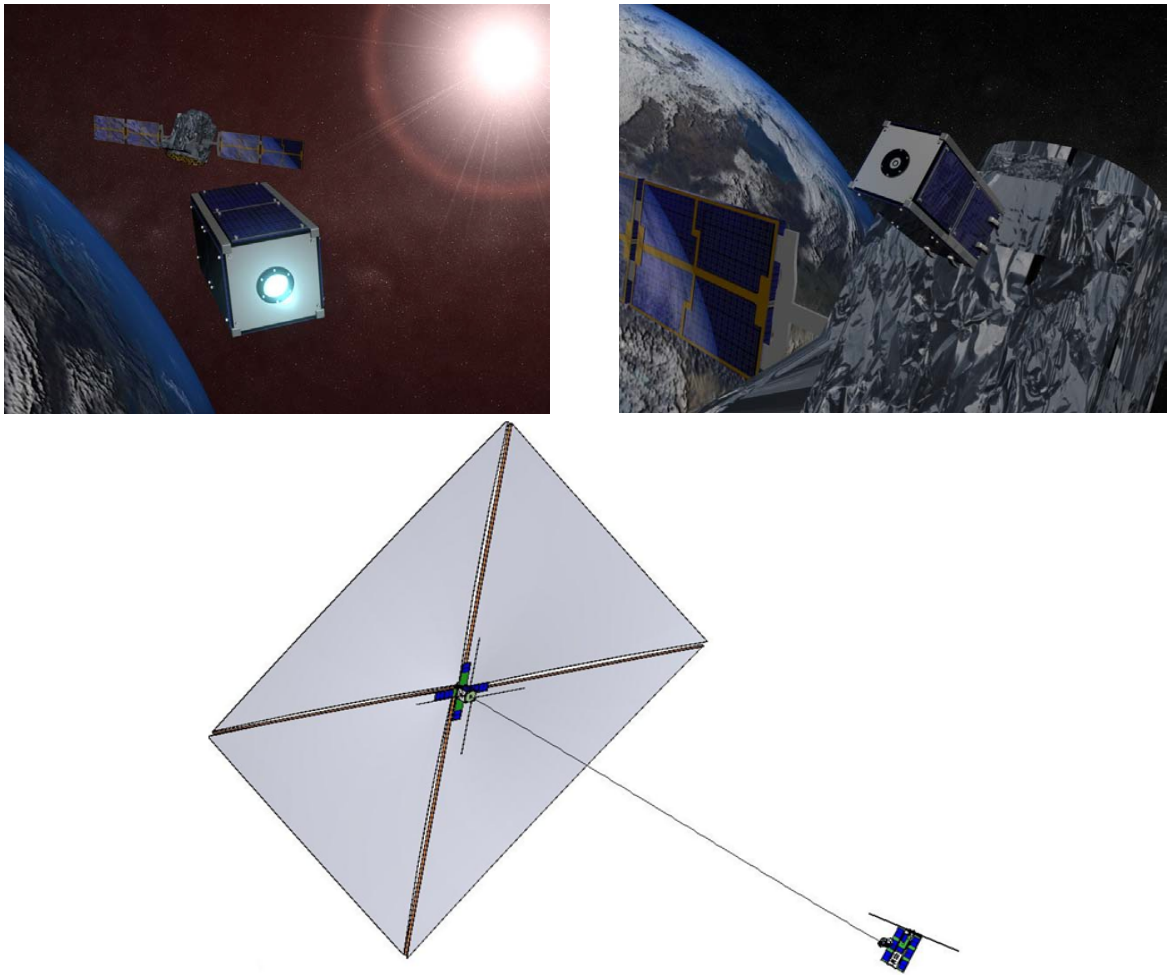

Figure 6 HybridSail docking and deployment

3 Theory

3.1 Aerodynamic drag

The presence of gas molecules in low Earth orbit results in both a disturbance force and a disturbance torque. The first will perturb the orbit of the satellite and cause the semi-major axis to decay over time, and the latter will influence the attitude of the satellite.

This study considers two different models for the aerodynamic drag force. The first is the widely accepted formula for atmospheric drag

$$\mathbf{F}_{drag} = -\frac{1}{2}\rho A C_d (\mathbf{v}_{rel}.\mathbf{v}_{rel}) \frac{\mathbf{v}_{rel}}{|\mathbf{v}_{rel}|} \quad 1$$

Where ρ is the density of the atmosphere, A is the area presented to the approaching molecules, C_d is the coefficient of drag (typically varies between 2.0 and 3.0 for a satellite) and $\mathbf{v}_{rel}$ is the velocity of the satellite relative to the atmosphere.

The above formula is an approximation that is often used when estimating orbit lifetime. It assumes hypervelocity, continuum flow [11]. It is also common to use the average cross-section area for a rotating satellite. For this study we will only consider the area of the sail membrane because the satellite body will be negligible compared to it. We also assume that the upper atmosphere rotates along with the Earth to give

$$\mathbf{v}_{rel} = \mathbf{v} + \mathbf{v}_{air} = \mathbf{v} + \boldsymbol{\omega}\times\mathbf{r} \qquad 2$$

Where $\mathbf{v}$ is the velocity of the satellite, $\mathbf{r}$ is the position vector and $\boldsymbol{\omega} = [0 \quad 0 \quad \omega]^T$ is the angular velocity vector of the Earth.

The second model for atmospheric drag will be used when studying the attitude of the satellite. The disturbing torque due to aerodynamic drag is given by the formula [12]:

$$\mathbf{N}_{aero} = \rho|\hat{\mathbf{v}}_{rel}|^2 A_p \left[\sigma_t(\mathbf{c}\times\hat{\mathbf{v}}_{rel}) + \left(\sigma_n\left(\frac{v_b}{|\mathbf{v}_{rel}|}\right) + (2-\sigma_n-\sigma_t)\cos\alpha\right)(\mathbf{c}\times\mathbf{n})\right] \qquad 3$$

Where

$\hat{\mathbf{v}}_{rel} = \frac{\mathbf{v}_{rel}}{|\mathbf{v}_{rel}|}$ is the local atmospheric unit vector

$\mathbf{c}$ is the centre-of-pressure vector relative to the satellite centre of mass

$\mathbf{n}$ is the normal vector of the sail (see explanation below)

σ_n and σ_t are the normal and tangential accommodation coefficients

$\frac{v_b}{|\mathbf{v}_{rel}|}$ is the ratio of molecular exit velocity to local atmospheric velocity

$\cos\alpha = \hat{\mathbf{v}}_{rel}\cdot\mathbf{n}$ is the cosine of the angle between the local velocity vector and the sail normal vector

The projected area, A_p, is calculated from

$$A_p = A\cos\alpha \qquad 4$$

Where A is the actual area of the sail.

To allow for situations where the sail flips over, the sail normal vector is chosen such that $\cos\alpha = \hat{\mathbf{v}}_{rel}\cdot\mathbf{n}$ is greater or equal to zero. If the dot product is negative, the negative of the sail normal is taken to ensure that the angle α will always be 90 degrees or smaller.

We will use the assumptions from [13]: $\sigma_n = \sigma_n = 0.8$ and $\frac{v_b}{|\mathbf{v}_{rel}|} = 0.05$

The atmospheric density is an important factor when evaluating drag. Various models exist for calculating atmospheric density with varying consideration of contributing factors. The simplest

static model assumes that the density varies exponentially with altitude. More sophisticated models make use of indices of solar and geomagnetic activity ($F_{10.7}$, a_p and K_p) to determine the time dependant density.

It was found that the input data to these models affects the accuracy just as much as the choice of the actual model [11]. It is therefore important to sufficiently estimate the solar and geomagnetic activity in order to model the atmosphere. Because propagations are carried out into the future and real data is not available in this case, the problem becomes estimating what the most likely trend will be.

The atmospheric model that was used in this study is the US Naval Research Laboratory NRLMSISE-00 model. It is particularly suited for space applications. The inputs to the model are:

- Current time
- Position
- $F_{10.7}$ solar flux index
- a_p geomagnetic index

Historic values for the $F_{10.7}$ and a_p indices are available, but for future dates these values have to be estimated. The estimation method that was followed in this study is described in [14]. The historic solar data was used to construct a pattern of mean values over one cycle for both indices. These mean cycles are then used for future dates, with a regression method to estimate the remainder of the current cycle.

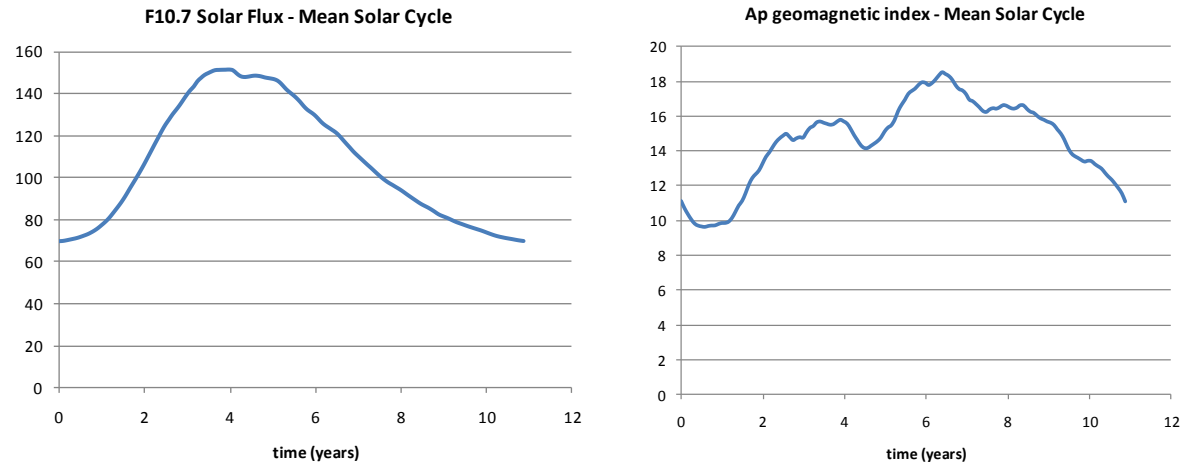

Figure 7 Mean solar flux and geomagnetic indices for use in atmospheric density estimation

3.2 Electrostatic tether

Tethers have proven to be a popular research topic for satellite de-orbiting. Different physical phenomena are exploited by the various tether types. Electrodynamic tethers make use of electromagnetic principles and can act either as electric power generators or as thrusters [15]. It relies on the motion of the satellite through a magnetic field.

The tether principle exploited in this study relies on the momentum exchange between a charged tether and the ionospheric plasma. This principle is described in [16]. The braking force that the tether will experience is given by:

$$\mathbf{F}_{electrostatic} = 1.72 P_{dyn} L \sqrt{\frac{\varepsilon_0 V_0}{e n_0}} e^{\left(\frac{-m_i |\mathbf{v}_{rel}|^2}{2eV_0}\right)} \frac{\mathbf{v}_{rel}}{|\mathbf{v}_{rel}|} \quad (5)$$

Where

$P_{dyn} = m_i n_0 |\mathbf{v}_{rel}|^2$ is the flow dynamic pressure

L is the tether length

n_0 is the ionosphere electron number density

m_i is the ionospheric mean ion mass

$\mathbf{v}_{rel}$ is the velocity of the spacecraft relative to the plasma

V_0 is the tether voltage

ε_0 is the permittivity of vacuum (8.854 x 10^{-12} $A^2s^4kg^{-1}m^{-3}$)

e is the charge of an electron (1.609 x 10^{-19} C)

The force calculation requires a model of the ionosphere. The International Reference Ionosphere 2007 (IRI-2007) model was used in this study to obtain the ion and electron densities.

3.3 Solar Radiation Pressure

Solar Radiation Pressure (SRP) is normally considered a disturbing force on the orbit of a satellite. This force can also work to our advantage when using the sail as a solar sail to perform orbit manoeuvres.

The solar radiation pressure forces are due to the momentum exchange of photons with the sail.

A portion of the photons that impact the sail are absorbed, and for the reflected photons, a portion is specularly reflected and the rest is diffusely reflected. Specular reflection is mirror-like reflection where the reflected photon always travels on a direction that is determined by the incoming direction. Diffuse reflection is reflection from a rough surface where the incident photon is seemingly reflected at a number of angles. The amount of photons that are absorbed, specularly and diffusely reflected are expressed as fractions.

$$\rho_a + \rho_d + \rho_s = 1 \quad (6)$$

From [17], the SRP force acting on a flat Lambertian surface at a distance of $r_\oplus$ = 1 AU from the sun is given by

$$\mathbf{F}_{r_\oplus} = PA(\mathbf{s} \cdot \mathbf{n}) \left\{ (1 - \rho_s)\mathbf{s} + \left[2\rho_s(\mathbf{s} \cdot \mathbf{n}) + \frac{2}{3}\rho_d \right] \mathbf{n} \right\} \quad (7)$$

Where P = 4.563 x 10-6 N/m^2 is the nominal solar-radiation-pressure constant 1 AU from the sun, A is the surface area of the sail, $\mathbf{n}$ is the normal vector to the sail surface and $\mathbf{s}$ is a unit vector pointing from the sun to the surface.

The SRP force for a distance other than 1 AU is obtained by correcting the solar-radiation-pressure constant,P , for the new solar distance, r. This results in a SRP force of

$$\mathbf{F}_{solar} = \left(\frac{r_{\oplus}}{r}\right)^2 PA(\mathbf{s}\cdot\mathbf{n})\left\{(1-\rho_s)\mathbf{s} + \left[2\rho_s(\mathbf{s}\cdot\mathbf{n}) + \frac{2}{3}\rho_d\right]\mathbf{n}\right\} \quad 8$$

We will be using equation (7) throughout this study because the orbits considered here all have an approximate sun distance of 1AU.

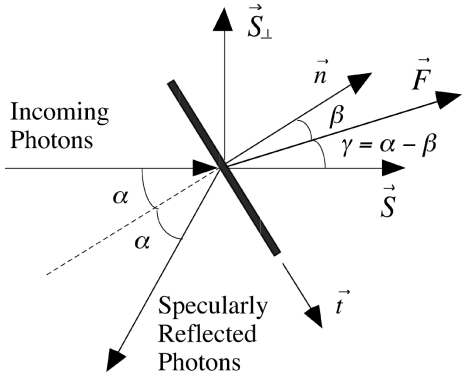

Figure 8 Solar Radiation Pressure normal and tangential components

Typical values for a reflective sail membrane are (from the optical properties described in [18])

$$\rho_a = 0.17 \quad \rho_s = 0.83 \quad \rho_d = 0 \quad 9$$

The disturbance torque caused by solar radiation pressure on the sail is given by

$$\mathbf{N}_{solar} = \mathbf{c}\times\mathbf{F}_{solar} \quad 10$$

Where $\mathbf{c}$ is the position vector from the satellite centre of mass to the centre-of-pressure of the sail.

3.4 Satellite orbit propagation

In order to examine the effectiveness of Hybridsail as a de-orbiting device, a means is required to accurately propagate the orbit of the satellite taking all the disturbing forces into account. The equation that describes the motion of a satellite in an inertial coordinate frame is [7]

$$\ddot{\mathbf{r}} = -\frac{\mu\mathbf{r}}{|\mathbf{r}|^3} + \mathbf{q} + \nabla V \quad 11$$

Where

$\mathbf{r}$ is the position vector from the centre of mass of the central body to the satellite

$\ddot{\mathbf{r}} = \frac{d^2\mathbf{r}}{dt^2}$ is the acceleration vector, $\mu = GM$ is the gravitational parameter for the central body, $\mathbf{q}$ is the acceleration due to non-conservative perturbing forces such as aerodynamic drag, solar radiation pressure (SRP) and electromagnetic forces and V is a potential function that describes the acceleration due to conservative perturbing forces (third-body point-mass and central body spherical harmonics).

Orbit propagation is carried out in the Earth-centred Inertial (ECI) coordinate frame, referenced to the J2000 epoch. Although the ECI frame is strictly not an inertial frame (the Earth is accelerating as it orbits around the Sun) equation (11) is still valid, as long as the third-body potential function includes the acceleration of the ECI frame (the second term in equation (14)).

Orbit propagation methods fall into three categories [8]:

1. Special perturbations orbit propagators based on numerical integration of the equations of motion
2. General perturbations orbit propagators that use analytic theories
3. Semi-analytic Satellite Theory (SST) propagators that use numerical integration to propagate mean element values and analytical models for the short-term periodic variations

The first method yields the most accurate results but requires small integration steps (typically 100 steps per revolution). Adaptive step sizes are usually employed when performing the numeric integration with the step size determined by the error bounds on the state and state derivatives. General perturbations propagators like the SGP4 orbit model can give quick results but suffers from inaccuracies due to inherent approximations [8]. The results also decay quickly when propagated far into the future relative to the time when the defining element sets were generated, although this is as a result of inaccuracies contained in the element set, not the propagation technique. Semi-analytic propagators can approach the accuracy of special perturbations propagators with the advantage of integrating over much larger time-steps (typically 1 day or longer).

Orbit propagation requires mathematical models for the perturbing effects, such as the central body gravitational potential, third body effects and non-conservative forces like drag and SRP.

Two different orbit propagators were implemented for this study. The first one performs numerical integration on the motion equations in Cartesian form (Cowell integration). The second uses Semi-analytical Satellite Theory to integrate the mean orbital elements. A reference implementation of the SGP4 orbit propagator was used to validate both methods.

3.4.1 Models

3.4.1.1 Earth gravity potential

The Earth gravity potential is modelled using spherical harmonics [9].

$$V_{Earth} = \frac{GM}{r}\left[1 + \sum_{n=2}^{N}\sum_{m=0}^{n}\left(\frac{a}{r}\right)^n \bar{P}_{nm}(\sin\phi)\left(\bar{C}_{nm}\cos m\lambda + \bar{S}_{nm}\sin m\lambda\right)\right] \quad 12$$

Where V is the gravitational potential function (m^2/s^2), GM is the gravitational parameter of the Earth, r is the distance from the satellite to the Earth's centre of mass, a is the semi-major axis of the WGS84 ellipsoid, C_{nm} and S_{nm} are the normalized gravitational constants and (r, ϕ, λ) is the position of the satellite in spherical coordinate representation.

$$\begin{aligned} r &= |\mathbf{r}| \\ \lambda &= \operatorname{atan2}(y, x) \\ \phi &= \tan^{-1}\left(\frac{Z}{r}\right) \end{aligned} \quad 13$$

The EGM96 (Earth Gravity Model 1996) coefficients were used in the model, up to order and degree 70.

3.4.1.2 Sun and Moon (third body) gravity potential

The sun and moon are modelled as point-masses. In this case, the disturbing potential becomes [7]

$$V_{third\ body} = \frac{\mu_3}{R_3}\left(\frac{R_3}{|\mathbf{R_3} - \mathbf{r}|} - \frac{\mathbf{R_3}.\mathbf{r}}{R_3^2}\right) \quad 14$$

With μ_3 equal to the third-body gravitational constant, $\mathbf{r}$ the position vector from the Earth centre of mass to the satellite and r the length of this vector, $\mathbf{R}_3$ the vector from the Earth centre of mass to the third body and R_3 the length of this vector.

The position of the sun is calculated by assuming an unperturbed elliptical motion of the Earth around the Sun, as described in [10]. The position of the moon relative to the Earth centre of mass is calculated using periodic terms, also described in [10].

3.4.1.3 Non-conservative forces

The non-conservative forces are described by the equations in section 3.1 to 3.3.

3.4.2 SGP4

SGP4 collectively refers to 5 mathematical models (SGP, SGP4, SDP4, SGP8 and SDP8) for predicting the perturbation effects on satellites in order to produce analytic solutions for satellite position and velocity vectors [19]. They are compatible with the two-line element sets produced by NORAD for all tracked Earth-orbiting objects.

The Simplified General Perturbations (SGP) models apply to satellites with an orbital period of 225 minutes or less. The position error of the SGP4 model is in the order of 1km at epoch and it grows by 1 to 3km per day. NORAD releases updated two-line elements for all tracked objects for this reason.

Simplified Deep-space Perturbations (SDP) models are used for satellites with higher orbits (period greater than 225 minutes) and assume a simplified drag model and add third-body (sun and moon) gravity effects.

Because of the availability of up-to-date two-line elements, the SGP4 models have become the standard for coarse satellite position determination.

The theory for the SGP4 models is contained in reference [19]. For this study, the reference code implementation from the Center for Space Standards & Innovation (CSSI) was used.

3.4.3 Cowell Integration

The state of the satellite is given by

$$\mathbf{x} = [\mathbf{r} \quad \dot{\mathbf{r}}]^T \quad 15$$

with $\mathbf{r} = [x \quad y \quad z]^T$ the position vector of the satellite in inertial Cartesian coordinates and $\dot{\mathbf{r}} = [v_x \quad v_y \quad v_z]^T$ the velocity.

The equation of motion then takes on the form of an initial value problem:

$$\mathbf{x}(t_0) = \mathbf{x}_0 \tag{16}$$

$$\frac{d\mathbf{x}}{dt} = f(t,\mathbf{x}) = \begin{bmatrix} \dot{\mathbf{r}} \\ \nabla V_{Earth} + \nabla V_{sun} + \nabla V_{moon} + \dfrac{\mathbf{F}_{sum}(t,\mathbf{x})}{m} \end{bmatrix}$$

Where m is the mass of the satellite, and

$$\mathbf{F}_{sum}(t,\mathbf{x}) = \mathbf{F}_{solar\ radiation\ pressure} + \mathbf{F}_{drag} + \mathbf{F}_{electrodynamic} \tag{17}$$

is the sum of all the forces acting on the satellite. Their values are calculated from the models described in sections 3.1 to 3.3

The gravity acceleration due to the Earth gravity potential is found by calculating the gradient

$$\nabla V_{Earth} = \left[\frac{\partial V_{Earth}}{\partial x} \quad \frac{\partial V_{Earth}}{\partial y} \quad \frac{\partial V_{Earth}}{\partial z}\right]^T \tag{18}$$

And similarly for the third bodies (Sun and moon)

$$\nabla V_3 = \left[\frac{\partial V_3}{\partial x} \quad \frac{\partial V_3}{\partial y} \quad \frac{\partial V_3}{\partial z}\right]^T \tag{19}$$

$$= \mu\left(\frac{\mathbf{R}_3 - \mathbf{r}}{|\mathbf{R}_3 - \mathbf{r}|^3} - \frac{\mathbf{R}_3}{R_3^3}\right)$$

The initial value problem in equation (16) can then be solved by any numeric ordinary difference equation method. For this implementation, the classical 4[th] order Runge-Kutta (RK) method was used with a fixed time step, h.

$$\begin{aligned} \mathbf{x}_{i+1} &= \mathbf{x}_i + \frac{h}{6}(\mathbf{k}_1 + 2\mathbf{k}_2 + 2\mathbf{k}_3 + \mathbf{k}_4) \\ \mathbf{k}_1 &= f(t_i, \mathbf{x}_i) \\ \mathbf{k}_2 &= f\left(t_i + \frac{h}{2}, \mathbf{x}_i + \frac{h}{2}\mathbf{k}_1\right) \\ \mathbf{k}_3 &= f\left(t_i + \frac{h}{2}, \mathbf{x}_i + \frac{h}{2}\mathbf{k}_2\right) \\ \mathbf{k}_4 &= f(t_i + h, \mathbf{x}_i + h\mathbf{k}_3) \end{aligned} \tag{20}$$

This choice was made because of the ease of implementation. An adaptive step-size RK method will yield a more optimal selection of the integration time step because then each time step is chosen to satisfy error bounds.

3.4.4 Semi-analytic Satellite Theory (SST)

Semi-analytic Satellite Theory, as used in this study, is described completely by reference [8]. This section is a short summary of the theory.

Semi-analytic Satellite Theory represents the state of the satellite as an equinoctial element set. The set consists of 6 elements, $(a_1, .., a_6)$. It relies on the equinoctial reference frame, defined by the 3 basis vectors $\mathbf{f}$, $\mathbf{g}$ and $\mathbf{w}$. These vectors have the following properties:

1. Vectors **f** and **g** lie in the orbital plane
2. **w** is parallel to the angular momentum vector of the satellite
3. The angle between **f** and the ascending node is equal to the longitude of the ascending node

There are 2 choices for **f** and **g** and this choice will determine whether the direct or retrograde equinoctial element set is being used. The 6 elements of the equinoctial element set are

$a_1 = a$ - the Keplerian semi-major axis

$(a_2, a_3) = (h, k)$ - the components of the eccentricity vector along **g** and **f** respectively

$(a_4, a_5) = (p, q)$ - the components of the ascending node vector along **g** and **f** respectively

$a_6 = \lambda$ - the mean longitude

The retrograde factor, I, determines whether the direct or retrograde equinoctial element set is being used. For the direct set, $I = 1$, and for the retrograde set $I = -1$. This choice is necessary to avoid singularities that exist at equatorial and polar orbits (inclination of 0° and 90°).

The first 5 elements are slowly varying with time, while the mean longitude is fast varying.

SST separates the osculating equinoctial elements into mean values and a remainder which varies periodically with the fast variable, λ.

$$\hat{a}_i = a_i + \eta_i(a_1, .., a_6, t) \quad (21)$$

Where $\hat{a}_i$ represents the osculating element and a_i the mean element.

The effect of orbital perturbations on the mean elements can be described by ordinary differential equations

$$\frac{da_i}{dt} = \delta_{i6} n + A_i(a_1, .., a_5, t) \quad (22)$$

Where $\delta_{ij} = 1$ if $i = j$ and 0 otherwise (Kronecker delta). n is the mean motion of the satellite. The short-period variations are described by Fourier series expressions

$$\eta_i = \sum_{j=1}^{\infty} \left[C_i^j(a_1, .., a_5, t) \cos j\lambda + S_i^j(a_1, .., a_5, t) \sin j\lambda \right] \quad (23)$$

Because the effect of perturbations on the mean elements are described by differential equations, the mean elements can be integrated numerically. Because the mean elements vary slowly, the integration time step can be quite long (typically a day or longer) – much longer than Cowell integration.

The same 4th order Runge Kutta scheme as in equation (20) was used for the implemented SST propagator. Because we are only interested in satellite orbit lifetime for this study (and not in accurate position at every time step) the short-period variations were omitted.

Reference [8] gives analytic expressions for all the contributions to the mean element differential equations for central body gravity potential, third body gravitational potential, aerodynamic drag and solar radiation pressure.

The effect of the electrostatic force generated by the HybridSail tether is modelled in the same way as atmospheric drag in SST. That is,

$$\frac{da_i}{dt} = \frac{1}{2\pi\sqrt{1-h^2-k^2}} \int_0^{2\pi} \left(\frac{r}{a}\right)^2 \left(\frac{\partial a_i}{\partial \dot{\mathbf{r}}} \cdot \mathbf{q}_{electrostatic}\right) dL \qquad 24$$

Where the integration spans over the true longitude, L. The perturbing acceleration due to electrostatic force is

$$\mathbf{q}_{electrostatic} = \frac{\mathbf{F}_{electrostatic}}{m} \qquad 25$$

Where m is the mass of the satellite, and $\mathbf{F}_{electrostatic}$ is the electrostatic force calculated from (5).

3.4.5 Validation of SST & Cowell methods

The following test orbit was used to validate the developed orbit propagation methods.

Satellite name	Sumbandila
Orbit	LEO with drag, circular sun-synchronous
Altitude	500 km
Eccentricity	0.0015
Mass	80 kg
Drag surface area	0.5 m^2
Two-line elements	1 35870U 09049F 11098.20453192 .00005047 00000-0 22680-3 0 7209 2 35870 097.2879 143.8695 0004132 128.5164 301.6107 15.21571712 86307

3.4.5.1 Cowell orbit propagator

The Cowell orbit propagator was initialized using position and velocity points from the SGP4 propagator. The reference SGP4 implementation was used to generate position and velocity at 10s intervals, for 1 orbit. The position and velocity at time t_0 was used as a first guess for the Cowell propagator state, and the Cowell integration was performed for one orbit. The position error was used to refine the initial condition until a best fit was achieved.

The graphs below shows the comparison between the SGP4 output and Cowell propagator output for 4 orbits.

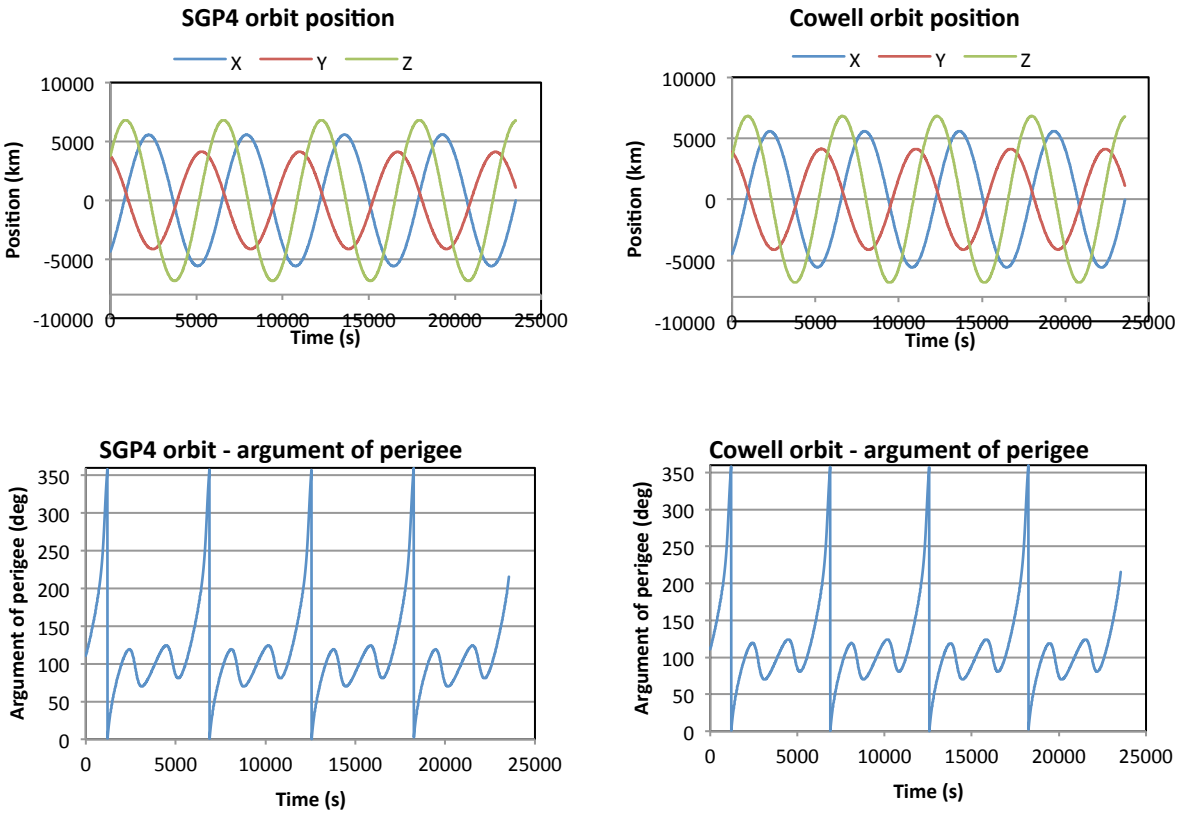

Figure 9 SGP4-Cowell orbit comparison (short-term)

The position error for the first 4 orbits is plotted below.

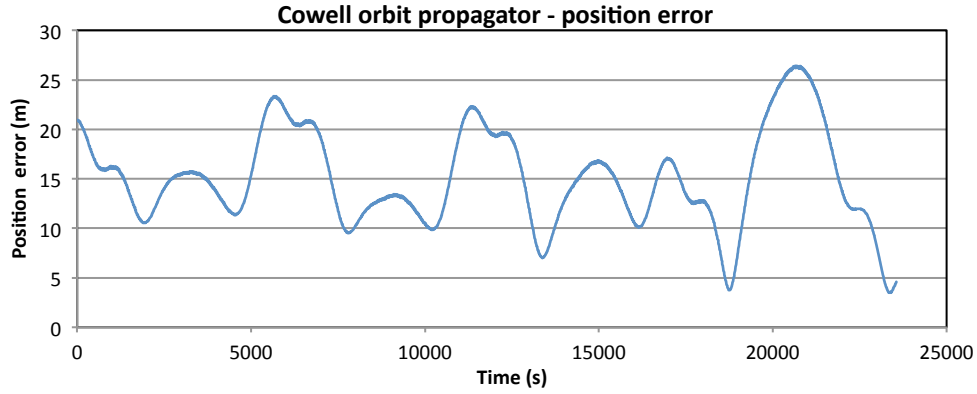

Figure 10 Cowell orbit propagator position error

If the propagation is carried on past this point, the position error begins to increase as expected due to numeric errors and the simplified models of SGP4. The trend for slowly varying parameters should still remain the same for both methods. The plots below show the semi-major axis and right-ascension of the ascending node for 1 month.

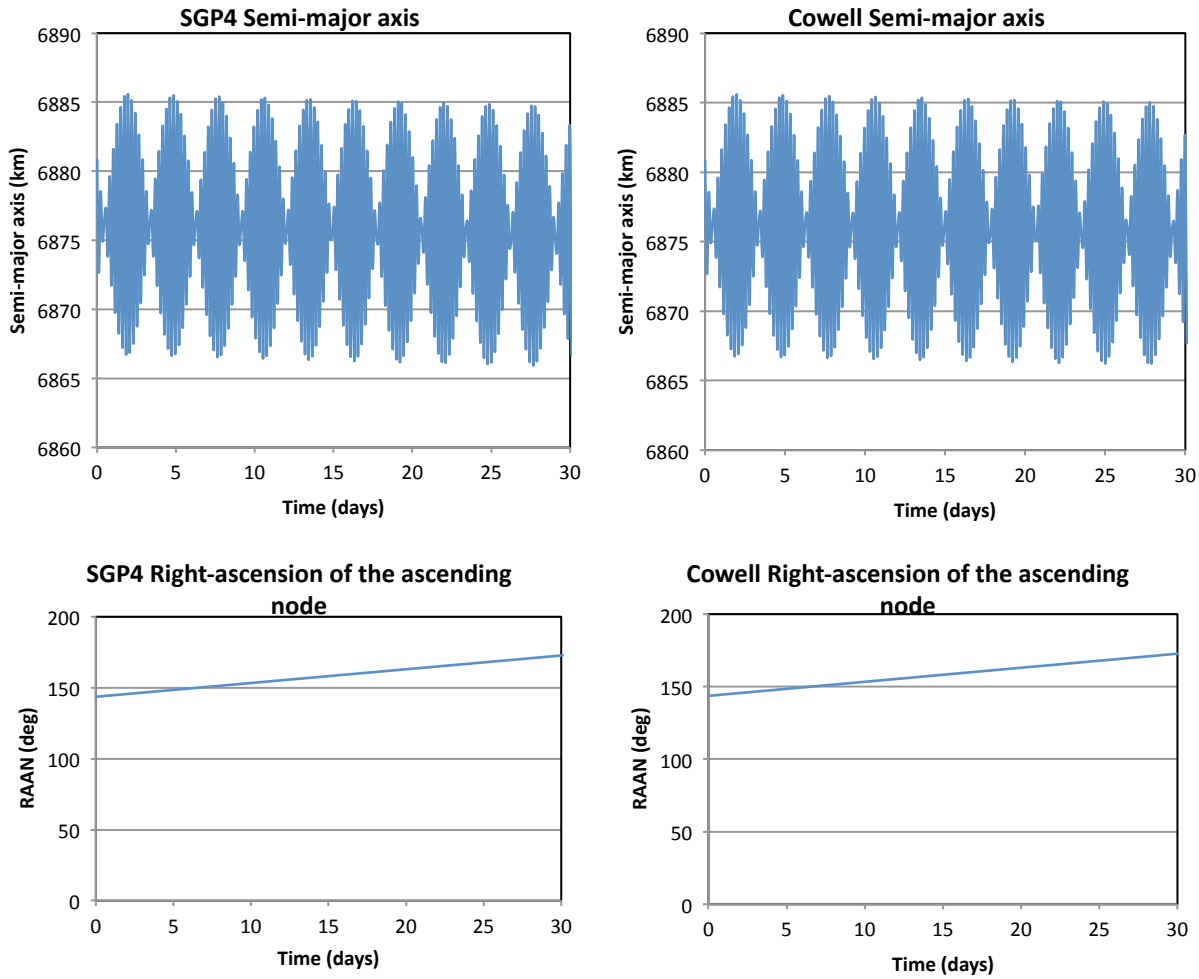

Figure 11 SGP4-Cowell orbit comparison (long-term)

3.4.5.2 Semi-analytic Satellite Theory propagator

The same initial SGP4 orbit as before was used to initialize the SST propagator. 50 data points spread out over 3 orbits was used to perform a regression fit to the initial mean elements.

Because the SST propagator only operates on the mean elements, a short term comparison with the SGP4 points is not possible. It is however possible to compare the slowly varying elements, taking into account that the SST orbital elements are mean elements with the osculating part removed.

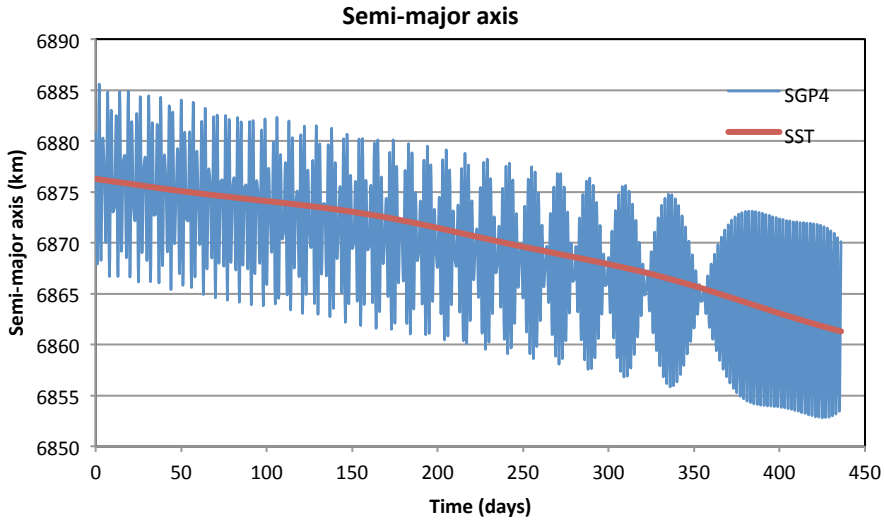

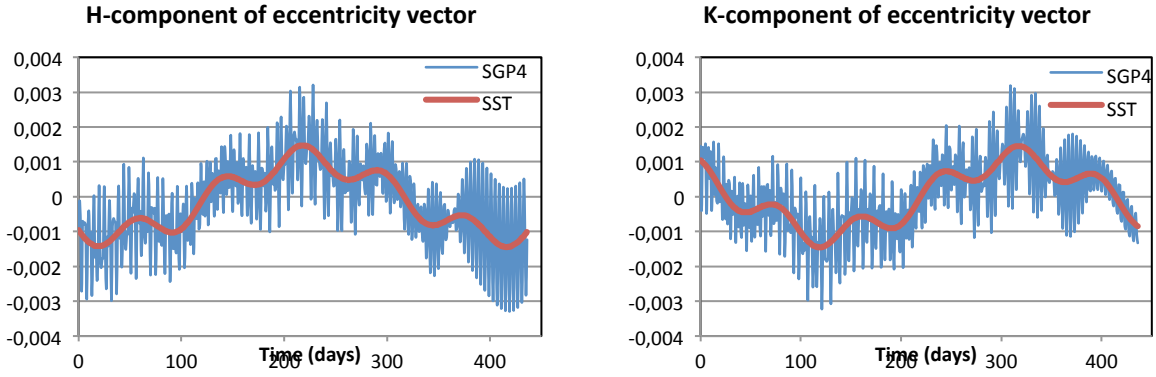

Figure 12 SGP4-SST orbit comparison

3.5 Attitude

3.5.1 Coordinate system definitions

The satellite coordinate system is defined as follows: the satellite body x-axis is aligned with the normal vector of the sail and the y- and z axes are aligned in the sail plane.

The satellite attitude is modelled in the orbit coordinate system. The orbit coordinate system rotates with the orbit so that the z reference axis points towards nadir, the x reference axis points towards the velocity vector and the y axis points along the orbit anti-normal. The satellite coordinate system will nominally be aligned with the orbit coordinate system when roll pitch and yaw equal 0.

The Earth-centered inertial coordinate frame (ECI) is used to propagate the position of the satellite and third bodies. A transformation is thus required to convert from ECI to orbit coordinate frames. This transformation can be obtained from the satellite position, $\mathbf{u}_I$, and velocity, $\mathbf{v}_I$, vector.

$$\mathbf{A}_{I/O} = \begin{bmatrix} \left(\mathbf{u}_I \times (\mathbf{v}_I \times \mathbf{u}_I)\right)^T \\ (\mathbf{v}_I \times \mathbf{u}_I)^T \\ -\mathbf{u}_I^T \end{bmatrix} \quad 26$$

3.5.2 Attitude representation

The spacecraft attitude is the transformation between the orbit coordinate frame and the satellite body frame. This transformation can be expressed as a quaternion, direction cosine matrix (DCM) or Euler angles.

When propagating the attitude we will make use of the quaternion representation to avoid singularities.

$$\mathbf{q}_{O/B} = [q_1 \quad q_2 \quad q_3 \quad q_4] \tag{27}$$

The quaternion attitude representation can be converted to a DCM using the following:

$$\mathbf{A}_{O/B} = \begin{bmatrix} q_1^2 - q_2^2 - q_3^2 - q_4^2 & 2(q_1q_2 + q_3q_4) & 2(q_1q_3 - q_2q_4) \\ 2(q_1q_2 - q_3q_4) & -q_1^2 + q_2^2 - q_3^2 + q_4^2 & 2(q_2q_3 + q_1q_4) \\ 2(q_1q_3 + q_2q_4) & 2(q_2q_3 - q_1q_4) & -q_1^2 - q_2^2 + q_3^2 + q_4^2 \end{bmatrix} \tag{28}$$

We will also express the attitude as pitch, θ, roll, ϕ, and yaw, ψ, Euler angles, defined as successive rotations. We will use a 2-1-3 rotation, so the pitch rotation takes place first. The Euler angles can be computed from the DCM and vice versa.

$$\begin{gathered} \theta = \operatorname{atan2}(A_{31}, A_{33}) \\ \phi = -\sin^{-1}(A_{32}) \\ \psi = \operatorname{atan2}(A_{12}, A_{22}) \end{gathered} \tag{29}$$

$$\mathbf{A}_{O/B} = \begin{bmatrix} C\psi C\theta + S\psi S\phi & S\psi C\phi & -C\psi S\theta + S\psi S\phi C\theta \\ -S\psi C\theta + CS\phi S & C\psi C\phi & S\psi S\theta + C\psi S\phi C\theta \\ C\phi S\theta & -S\phi & C\phi C\theta \end{bmatrix} \tag{30}$$

Where C is the cosine function and S the sine function.

3.5.3 Attitude propagation

The orbit referenced body rate vector, $\boldsymbol{\omega}_B^O = [\omega_{xo} \quad \omega_{yo} \quad \omega_{zo}]^T$, (the rotation rate of the spacecraft body frame relative to the orbit reference frame) is used to propagate the quaternion attitude.

$$\begin{bmatrix} \dot{q}_1 \\ \dot{q}_2 \\ \dot{q}_3 \\ \dot{q}_4 \end{bmatrix} = \frac{1}{2} \begin{bmatrix} 0 & \omega_{zo} & -\omega_{yo} & \omega_{xo} \\ -\omega_{zo} & 0 & \omega_{xo} & \omega_{yo} \\ \omega_{yo} & -\omega_{xo} & 0 & \omega_{zo} \\ -\omega_{xo} & -\omega_{yo} & -\omega_{zo} & 0 \end{bmatrix} \begin{bmatrix} q_1 \\ q_2 \\ q_3 \\ q_4 \end{bmatrix} \tag{31}$$

The relationship between the orbit referenced body rates and inertially referenced body rates, $\boldsymbol{\omega}_B^I$, is given by

$$\boldsymbol{\omega}_B^I = \boldsymbol{\omega}_B^O + \mathbf{A}_{O/B}[0 \quad -\omega_o \quad 0]^T \tag{32}$$

Where $\omega_o = \sqrt{\frac{\mu}{|\mathbf{r}|^3}}$ is the orbit angular rate.

The attitude dynamics equation gives the rate of change of the inertially referenced body rates.

$$\mathbf{I}\dot{\boldsymbol{\omega}}_B^I = \sum_i \mathbf{N}_i - \boldsymbol{\omega}_B^I \times \mathbf{I}\boldsymbol{\omega}_B^I \quad (33)$$

Where $\sum_i \mathbf{N}_i$ is the sum of all the disturbance and control torques on the satellite and $\mathbf{I}$ is the moment of inertia tensor.

The disturbance torques that will be taken into consideration are the aerodynamic disturbance torque from equation (3), solar radiation pressure disturbance torque (equation 10) and gravity gradient torque.

Rotations take place about the centre-of-mass of the satellite. The aerodynamic and solar radiation pressure torques are moments caused by the solar radiation force and aerodynamic force. These forces are applied at the centre-of-pressure of the sail, and the lever arm (connecting the centre-of-mass to the point where the force is applied) is the position vector from the centre-of-mass to the centre-of-pressure.

The gravity gradient torque, $\mathbf{N}_{GG}$, is given by:

$$\mathbf{N}_{GG} = 3\omega_o^2(\mathbf{z}_o^B \times \mathbf{I}\mathbf{z}_o^B) \quad (34)$$

The vector $\mathbf{z}_o^B$ is the orbit nadir vector in body coordinates.

$$\mathbf{z}_o^B = \mathbf{A}_{O/B}[0 \quad 0 \quad 1]^T \quad (35)$$

The attitude state can be propagated using a numerical integration method, using the differential equations of (31) and (33) and some initial state for the attitude and orbit referenced body rates.

A modified Euler integration scheme (pyramid integration) was used to propagate the attitude for this study.

4 Satellite de-orbit analysis

This section will investigate the effectiveness of HybridSail as a de-orbiting device, as well as the applications where it can be used and the parameters that influence the effectiveness. For this purpose the time to de-orbit is evaluated and compared for the criteria under investigation.

The de-orbit time is the time it takes for a satellite to reach a post-mission disposal orbit. For this study we consider only LEO satellites that are affected by drag and Geosynchronous Earth Orbit (GEO) satellites. The latter can be de-orbited using the sail as a solar sail, and in the first case the satellite can be de-orbited using a combination of aerodynamic drag and electrostatic braking.

For a de-orbit strategy to be considered effective, the de-orbit time has to be below 25 years from the spacecraft end-of-life, to comply with [6].

The first sub-section (4.1) will evaluate only aerodynamic drag augmentation. The next (4.2) will investigate the capabilities of electrostatic tethers as a de-orbiting means. Section 4.3 considers the combined effect of drag de-orbiting augmented with tethers. Section 4.4 looks at the collision probability of a sail in its de-orbiting phase and section 4.5 looks at the option of using the sail as a solar sail to propel the host satellite to a higher graveyard orbit.

Only in section 4.5 is the solar force used constructively to de-orbit. In all other cases the sail is used purely as a drag augmentation device although the disturbing effect of solar radiation pressure is still considered throughout.

4.1 Drag sail de-orbiting in LEO

Aerodynamic drag augmentation is achieved by maximizing the surface area perpendicular to the satellite velocity. This is depicted in the image below.

Figure 13 Aerodynamic drag sail de-orbiting

In this case the attitude of the sail remains constant. Attitude is the orientation of the satellite body relative to the orbit coordinate system. For the attitude to remain constant the satellite has to rotate once per obit relative to an inertial reference frame.

4.1.1 Solar activity

Solar activity plays a significant role in atmospheric models. It has been observed that there is a day-night variation in the density of the upper atmosphere, sometimes referred to as the “diurnal bulge”. The bulge has a peak around 2p.m. local solar time and a minimum around 4a.m. [20]. But is has also been found that the 11-year cyclic variation in solar activity influences the density of the atmosphere.

The daily variations in atmospheric density is such that the effect on aerodynamic drag over a long time period can be approximated by an average density, but the 11 year solar cycle can significantly influence de-orbit times.

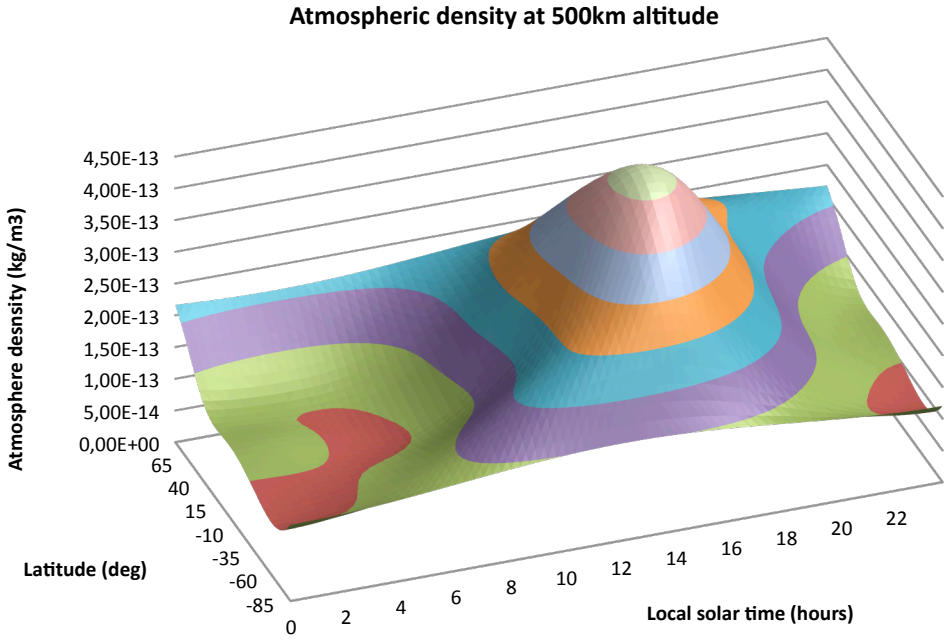

Figure 14 Atmospheric density at 500km altitude showing the diurnal bulge

Most atmospheric models take as input indices that reflect the current solar activity. The most widely used indices are the $F_{10.7}$ solar flux and a_p or K_p geomagnetic indices. These values are recorded by observatories over the world and historic data is readily available, but for future predicted solar activity, an estimation algorithm is required, such as the one described in section 3.1.

The difference in density as a result of solar activity is illustrated by plotting the atmospheric density per altitude at the maximum and minimum epoch. The last minimum and maximum epochs were used.

Table 4-1 Previous solar minimum and maximum

	Date	**a_p index**	**$F_{10.7}$ index**
Solar min	December 2008	4.9	68.5
Solar max	February 2002	12.1	196.8

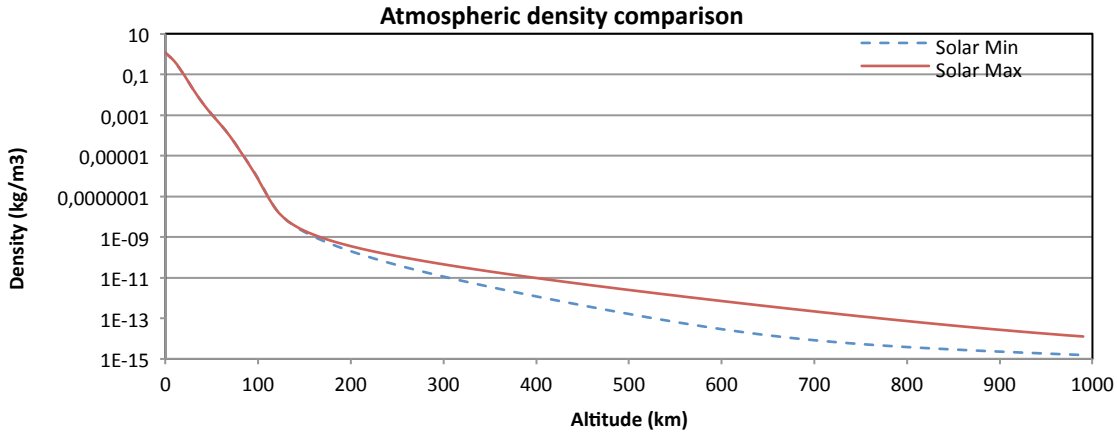

Figure 15 Atmospheric density as a function of altitude at solar max and min (0 deg longitude, 0 deg latitude, 12p.m. local solar time)

The density at solar maximum can sometimes be more than 20 times that at corresponding conditions at solar minimum. The effect can further be demonstrated by comparing de-orbit times under differing solar conditions. The following table shows de-orbit times for the same satellite, starting to de-orbit at solar maximum and solar minimum. It also shows the ratio of the two de-orbiting times.

Table 4-2 Comparison of de-orbit times starting at solar maximum and minimum epochs

Sail size (m^2)	De-orbit time starting at solar max (days)	De-orbit time starting at solar min (days)	Ratio of solar min de-orbit time vs. solar max
400	4.0	86.8	21.7
100	15.8	346	21.9
25	58.5	1007	17.2
10	163.5	1561	9.5
5	412.5	2294	5.6
2	3680	5270	1.4
1	7754	8235	1.1

The parameters for the simulation in the above table are:

Physical parameters	
Satellite mass	100 kg
Initial orbit	
Altitude	600 km
Eccentricity	0.001
Inclination	97.77 deg

The plot below shows how the ratio of the de-orbiting times change as a function of the solar max de-orbit time. It can be seen that only when the time to de-orbit is in the order of two times the solar cycle duration (>20 years) will the effect of solar activity even out and the starting point of de-orbitation not play a role anymore.

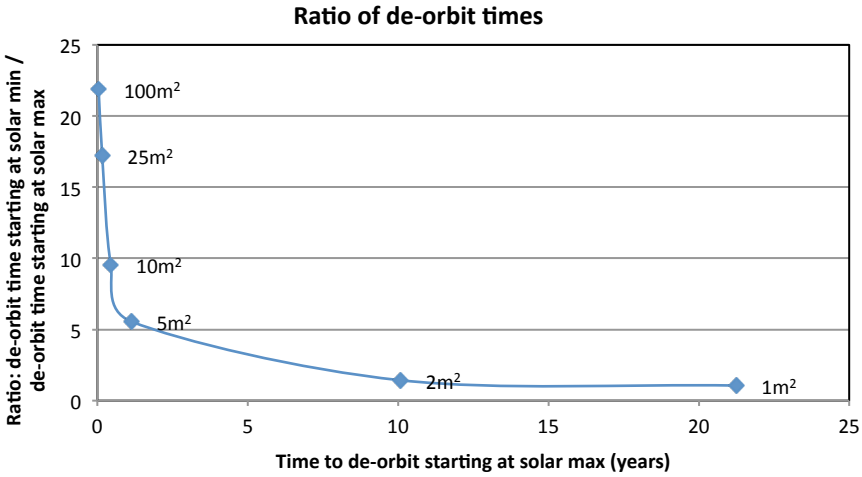

Figure 16 Ratio of solar maximum and minimum de-orbit times

4.1.2 Sail sizing

The parameters that influences the de-orbit time of a drag sail is the physical satellite parameters (mass and sail area) and the initial orbit (altitude, eccentricity, inclination).

To evaluate the effect of the physical satellite parameters, we note that the acceleration due to the drag force is a function of sail area over satellite mass.

$$\mathbf{a}_{drag} = \frac{\mathbf{F}_{drag}}{m} = \frac{\rho A C_d}{2m} (\mathbf{v}_{rel} . \mathbf{v}_{rel}) \frac{\mathbf{v}_{rel}}{|\mathbf{v}_{rel}|} \quad 36$$

The ballistics coefficient, $BC = \frac{m}{AC_d}$, is often used to describe this relation. Because the sail area scales together with the mass, it is only necessary to find the desired ballistics coefficient for a certain scenario and the sail area can be selected given the mass of the satellite. The table below shows the ballistics coefficient for a few sail sizes and satellite masses. A drag coefficient, C_d, of 2.2 is assumed throughout.

Table 4-3 Ballistics coefficient as a function of mass and sail area

Ballistics Coefficient (kg/m²)		Satellite mass (kg)			
		100	500	1000	5000
Sail area (m²)	10	4.5	11.4	45.5	227.3
	25	1.8	4.5	18.2	90.9
	100	0.5	1.1	4.5	22.7
	400	0.1	0.2	0.9	4.5

To simplify the analysis, we consider circular orbits at various altitudes. Also, the initial inclination for the orbit is chosen so that the orbit is sun-synchronous. That is, it will have a nodal precession rate equal to the rate at which the earth rotates around the sun. Consequently the satellite will have the same lighting conditions every orbit, and thus the same atmospheric density profile.
The graphs below show the de-orbit times as a function of initial altitude and ballistics coefficient. The plotted de-orbit times are the averages taken from a solar maximum and solar minimum starting point.

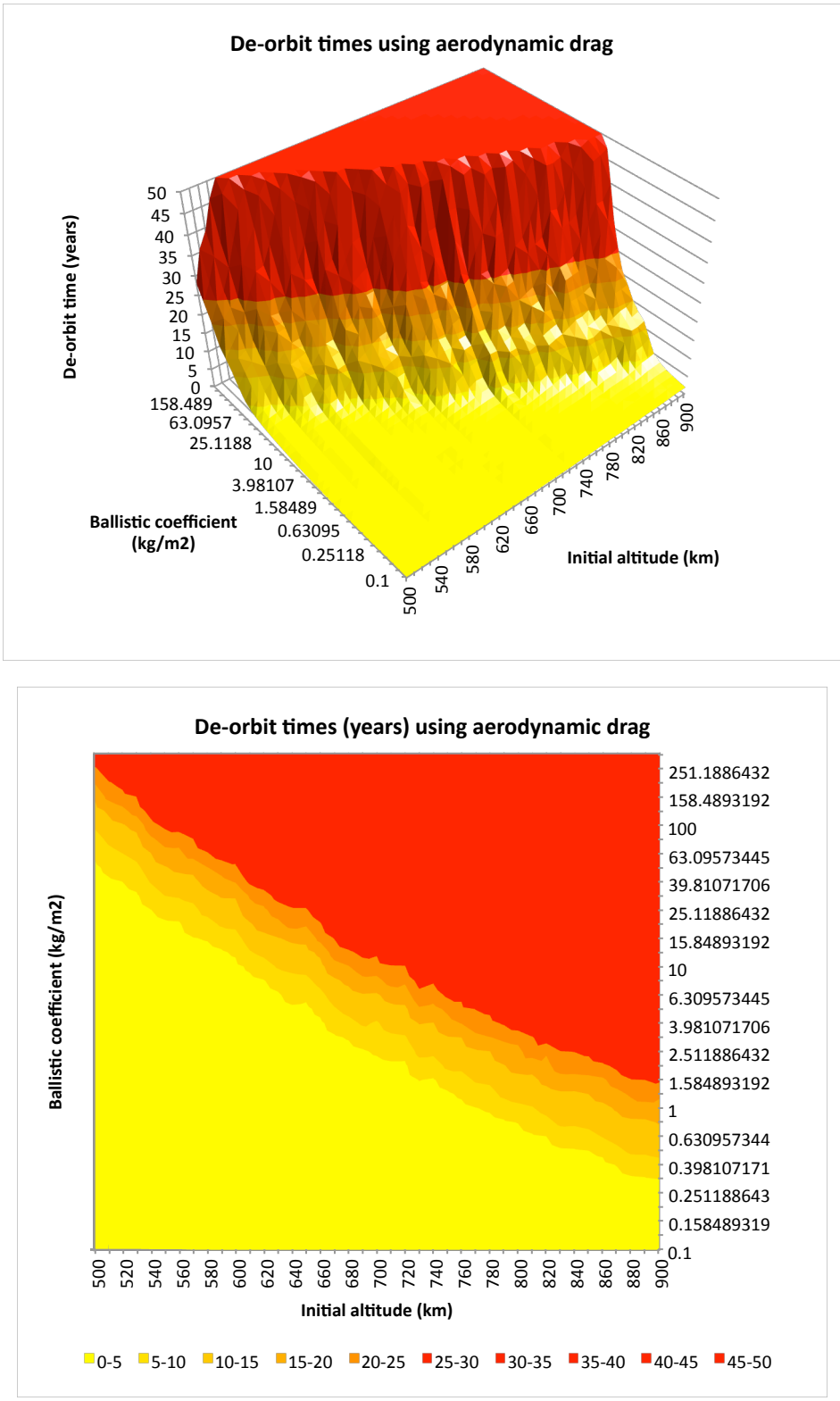

Figure 17 De-orbit times using aerodynamic drag

From the above plot, it is possible to select the required sail size for a given satellite mass and initial altitude. For instance, to de-orbit within 25 years from an initial 900km circular orbit, a ballistics coefficient of 1.6 is needed. If the mass of the satellite is know, the sail area can be calculated from

$$A = \frac{m}{BC.C_d} \quad (37)$$

4.1.3 Orbit Eccentricity

As an orbit becomes more eccentric the variation in atmospheric density over an orbit becomes more pronounced. High Eccentricity Orbits (HEO) may have a perigee altitude in the LEO region, but apogee altitude far above the atmosphere such that the satellite passes in and out of the atmosphere during every orbit.

The resulting effect is that the orbit will become more circular over time. The graph below illustrates this. The satellite and initial orbit has the following parameters

Satellite Physical parameters	
Ballistic coefficient	1.8
Initial Orbit	
Eccentricity	0.4
Semi-major axis	11300 km
Altitude at perigee	400 km
Altitude at apogee	9450 km

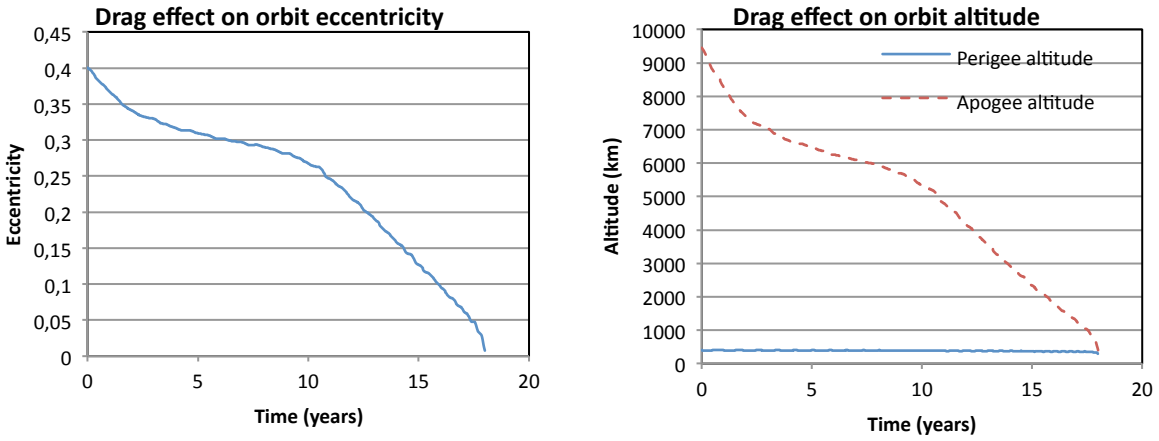

Figure 18 Effect of aerodynamic drag on orbit eccentricity

It is then expected that the de-orbit time for orbits with the same perigee altitude will increase as a function of orbital eccentricity. The plot below gives the de-orbit times as a function of eccentricity for an orbit with perigee altitude of 500km. The ballistics coefficient is 1.8.

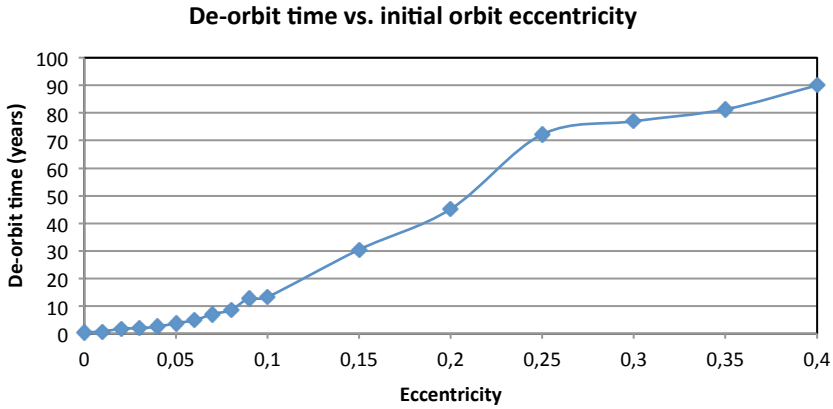

Figure 19 De-orbit time as a function of initial orbit eccentricity

4.2 Electrostatic de-orbiting in LEO

4.2.1 Solar activity

Solar activity not only affects the atmospheric density, it also changes the ion composition of the ionosphere.

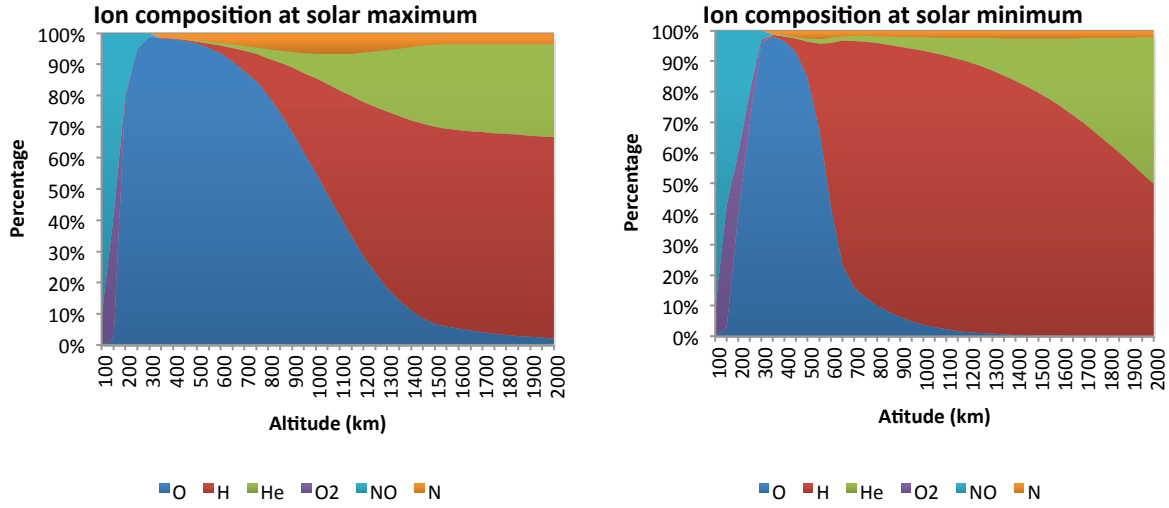

Figure 20 Differences in ion composition at solar maximum and minimum epochs

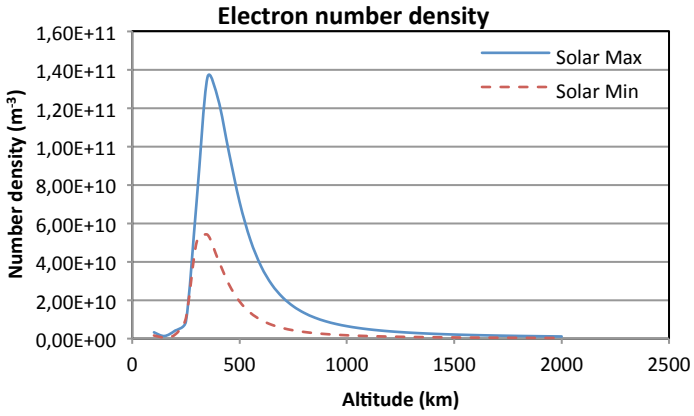

Figure 21 Differences in electron density at solar maximum and minimum epochs

The effect of solar activity on electrostatic tether de-orbiting is similar to drag de-orbiting. If the time to de-orbit is longer than the 11 year solar cycle, the effect averages and the starting point of de-orbitation does not play a role in the eventual de-orbit time. But it can be noticed that even for very short de-orbit times the ratio of de-orbit time at solar min to de-orbit time at solar max is not as great as with drag de-orbiting.

Table 4-4 Comparison of de-orbit times starting at solar maximum and minimum epochs

Total tether length (m)	De-orbit time starting at solar max (days)	De-orbit time starting at solar min (days)	Ratio of solar min de-orbit time vs. solar max
20000	450	700	1.6
10000	840	1180	1.4
5000	1700	1880	1.1
2000	3320	3460	1.0
1000	5520	5700	1.0

The parameters for the simulation in the above table are:

Physical parameters	
Satellite mass	100 kg
Tether voltage	100 V
Drag area	0.5 m^2
Initial orbit	
Altitude	600 km
Eccentricity	0.001
Inclination	97.77 deg

4.2.2 Tether Parameters

Considering equation (5), the physical parameters that can be specified in the spacecraft design is the tether voltage and the total tether length. Although the tether length can potentially be scaled to any length, there are implications to the power supply and deployment system. Instead of

assuming a scalable tether design, we rather limit the study to 3 specific designs. Their parameters are summarized in the table below:

Table 5 Tether satellite design parameters

	1	2	3
Voltage (V)	150	1000	4000
Total Tether Length (m)	400	1600	6400

The de-orbit capabilities of the 3 tether satellite designs are illustrated by the graphs below. Each graph shows the time to de-orbit as a function of initial altitude, for 3 different satellite masses. The orbits were initially circular sun-synchronous orbits.

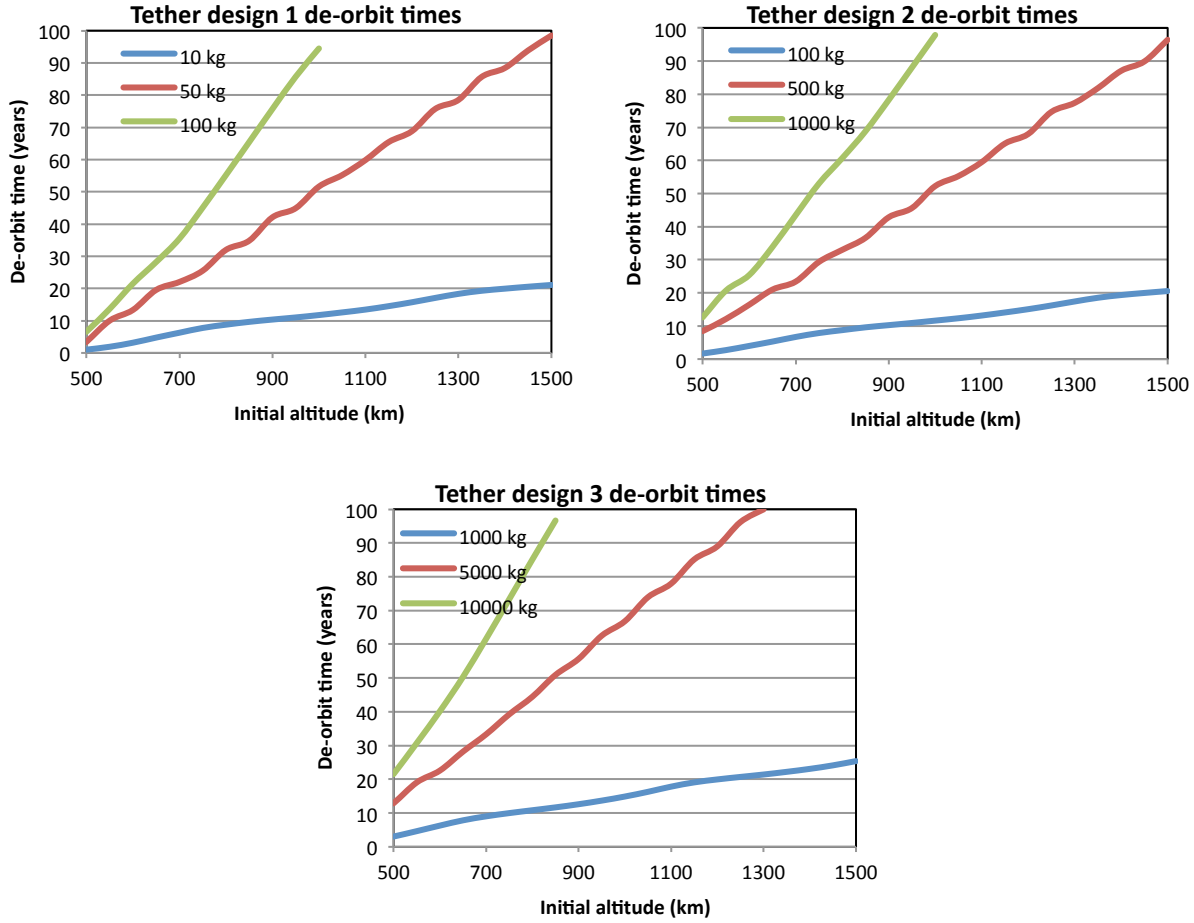

Figure 22 Tether satellite de-orbit times

4.3 Combined sail-tether de-orbiting in LEO

It can be seen that tether satellites poses the added advantage of de-orbiting capability at higher altitudes than aerodynamic drag. It therefore makes sense to augment the de-orbiting capabilities of a sail with tethers to increase the altitude range over which it can be used. To illustrate the enhancement, we use the same 3 tether satellite designs as before and augment it with a square drag sail.

Table 6 Combined sail-tether satellite design parameters

	1	2	3
Voltage (V)	150	1000	4000

Total Tether Length (m)	400	1600	6400
Sail Area (m^2)	25	400	1600

The time to de-orbit with the added sail is plotted in the graphs below

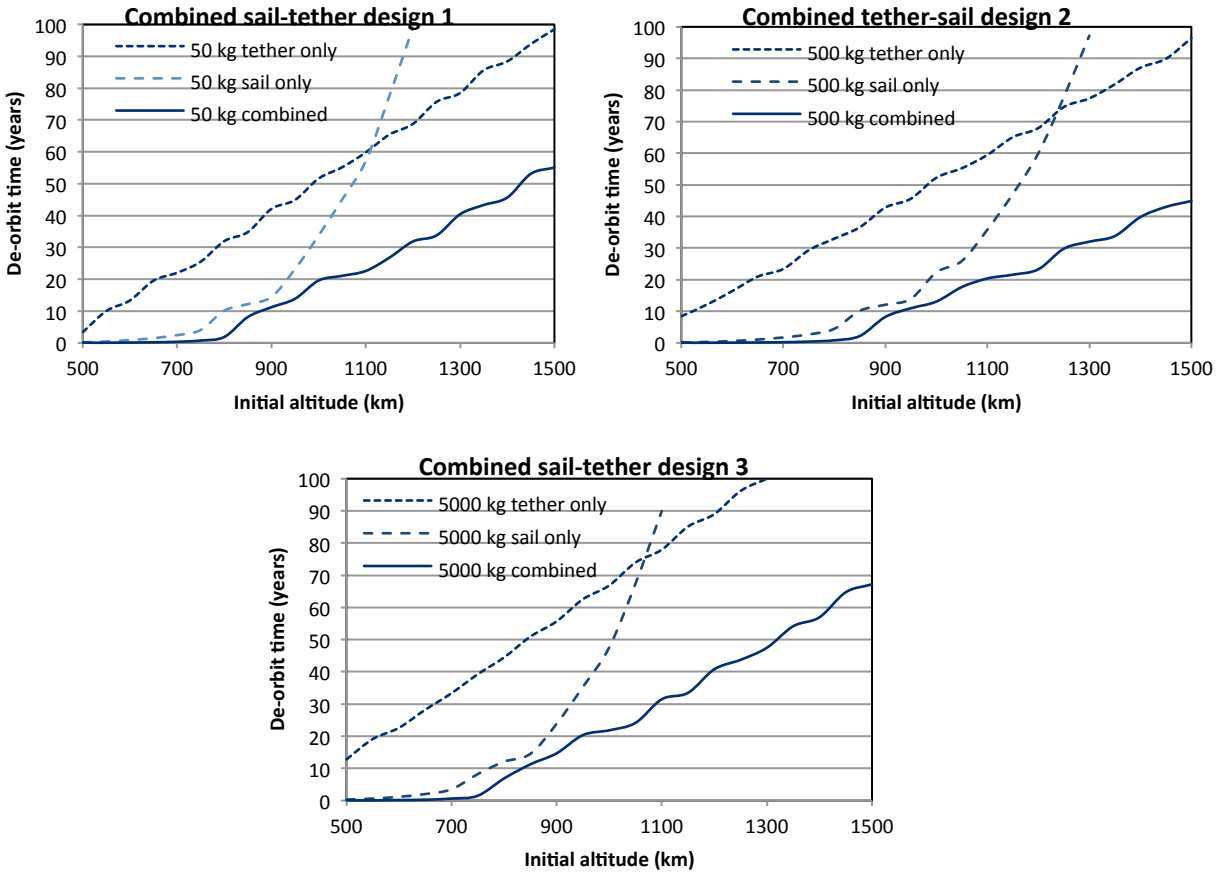

4.4 Collision probability

The method of [21] was used to calculate the probability of a collision for the sail satellite during its de-orbiting phase. The volume surrounding the LEO region was sub-divided into smaller volume segments, but instead of the spherical volume sections proposed in [21], the cube regions of [22] were used.

We used a recent version of the www.space-track.org catalogue of published Two Line Elements (TLE's) – 23 March 2011. For each satellite in the catalogue, a series of passage events were recorded for every cube volume. A single cell passage event is described by the spatial density of the satellite and the velocity at which it passes through the volume element. This forms a constant debris population, unlike [22] where the orbital decay of debris and new launches are considered.

When propagating the orbit of the sail satellite, the probability of a collision with another debris satellite in the same volume segment is given by

$$P_i = s_i s_{sail} V_{rel} \sigma dU \qquad 38$$

Where

P_i is the probability of a collision between the sail and satellite i,

s_i is the spatial density of satellite i in the volume segment,

s_{sail} is the spatial density of the sail satellite in the volume segment,

V_{rel} is the relative velocity between the two satellites

σ is the collision cross section area and

dU is the volume of the cube

To obtain the collision probability for an entire orbit, the above is equation is summed over all the cubes through which the sail passes and for all the satellites that passes through the same cube. At every integrator time-step, the collision probability is evaluated for a single orbit, and multiplied by the number of orbits in the integrator time-step. This allows us to calculate the total collision probability for the satellite over its de-orbiting span. The plot below shows how the collision probability changes over time for a satellite that de-orbits from a 900km circular orbit. The initial inclination was 23.8 degrees.

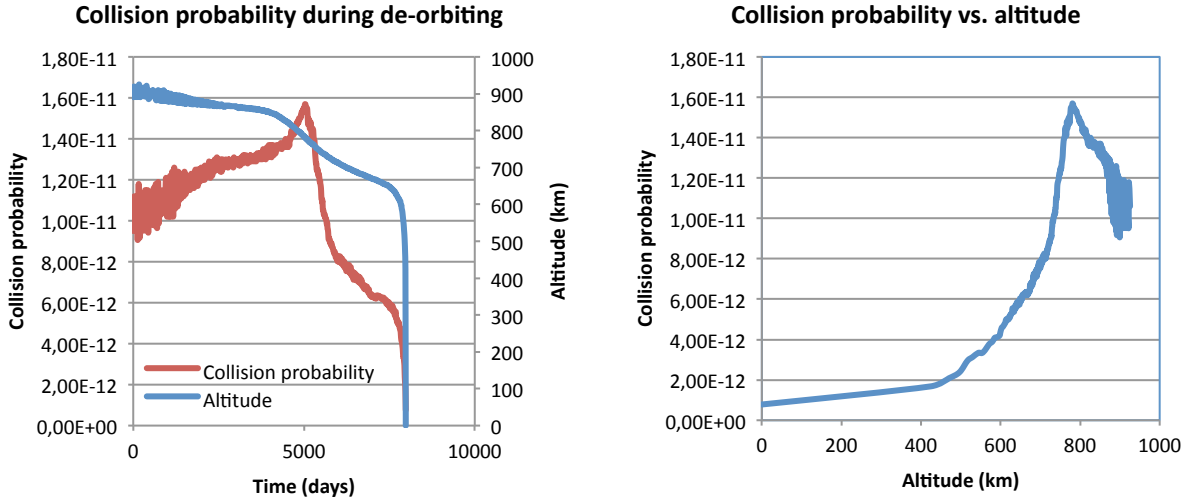

Figure 23 Collision probability during de-orbiting

It can be seen that the collision probability is a maximum at an altitude of 770km. This corresponds to the altitude distribution of objects in LEO (Figure 3) which also has a peak at this altitude.

When calculating the collision probability for the 2 sample orbits from [21], the following results are obtained:

Test case	Orbit	Lifetime	Cross-section	Result from [21]	Our result
ARISTOTELES	92.3° inclination, 475 km	4 years	10 m^2	0.07%	0.13%
Space Station	28.5° inclination, 450 km	30 years	150 m^2	3.3%	8.6%

The higher collision probability in this work can be contributed to the larger number of orbiting objects in the 2011 catalogue (10600 vs. 6600 in [21]). We used the same factor (20x) to estimate the number of uncatalogued objects that may cause catastrophic collisions.

Using this approach, we can compare the collision probability for various de-orbiting scenarios. The graphs below show the total collision probability over the satellite lifetime as a function of sail area (ballistic coefficient) for a 1000kg satellite, starting to de-orbit from 600km and 800km circular orbits.

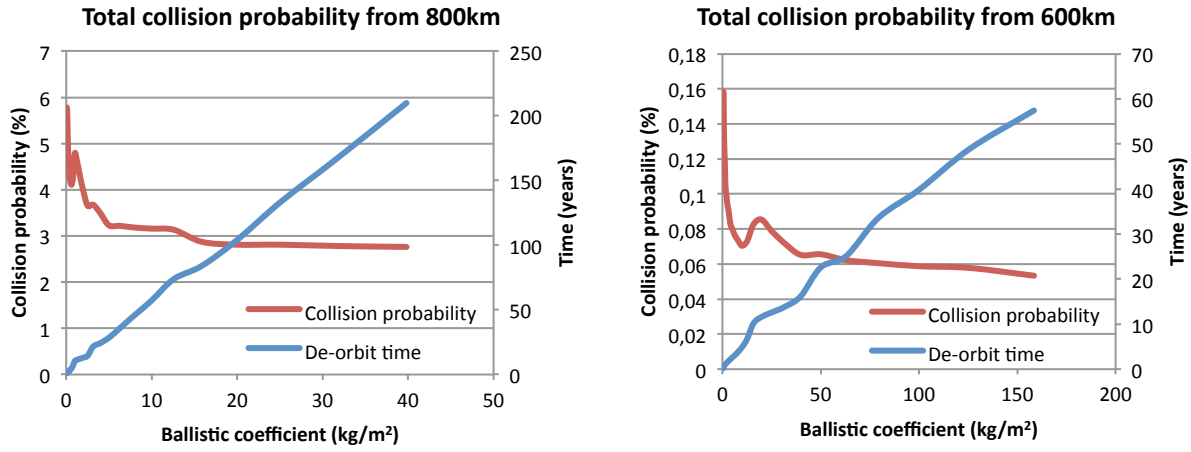

Figure 24 Total collision probability as a function of sail size

The graphs above show that although a larger surface area leads to a quicker de-orbiting time, the total collision probability is larger. It should be noted however that in equation (38) the collision cross section area is taken only as the area of the HybridSail satellite and does not take into account the area of the debris piece (because this information is not available). As the test satellite's area becomes smaller (ballistic coefficient becomes larger) the size of the debris pieces should play an increasing role in collision cross section area and this is not reflected in the graphs of Figure 24.

The above results also do not take the different kind of collision failures into account. For small debris pieces that impact the sail, the likely result will be a ripped sail. But the sail can be designed to prevent the rip from propagating further, and the sail can still function as before. Larger pieces of debris might destroy a complete sail segment, leaving other segments intact. In this case the satellite will start to tumble but it will still have some de-orbiting capability. If the satellite bus is impacted the entire HybridSail satellite will be lost.

We can conclude from the above figure that it is better to choose the sail as small as possible to result in a 25 year de-orbit time rather than a larger sail with shorter de-orbit time.

4.5 Solar sailing orbit manoeuvres

Most solar sailing missions target applications outside of normal Earth orbits. This is due to the essentially unlimited delta-V that solar radiation pressure force offers and this enables missions that would otherwise be less feasible. Examples of such missions include inner and outer solar system rendezvous and flyby missions, sun centred orbits and Earth escape trajectories [35].

A small number of planet-centred applications have been proposed, but a big restriction on this type of application is the attitude control demands. The section below describes a control technique to

perform an orbit manoeuvre to move to a higher orbit from the GEO belt, although the technique can potentially be used for other orbit types as well.

Other Earth centred solar sailing methods include Earth escape trajectories [38], lunar fly-bys [37], and the proposed GeoStorm mission to monitor the Earth's magnetotail [36]. Optimal trajectories between orbits have also been researched [39][41]. A general control method for Earth-centred solar sailing orbit transfers and station keeping has been proposed by Macdonald and McInnes [40].

4.5.1 Solar sail de-orbiting in GEO

Aerodynamic drag stops being useful above 1000km where the atmospheric density becomes insignificant. A large surface area sail can be used not only as a drag augmentation device but the solar radiation pressure generated on it can also be used for orbit manoeuvres.

Satellites in geosynchronous Earth orbit (GEO) are disposed by placing them in an orbit with perigee 300km above GEO. The mechanism by which a solar sail would achieve a higher orbit is illustrated in the figure below.

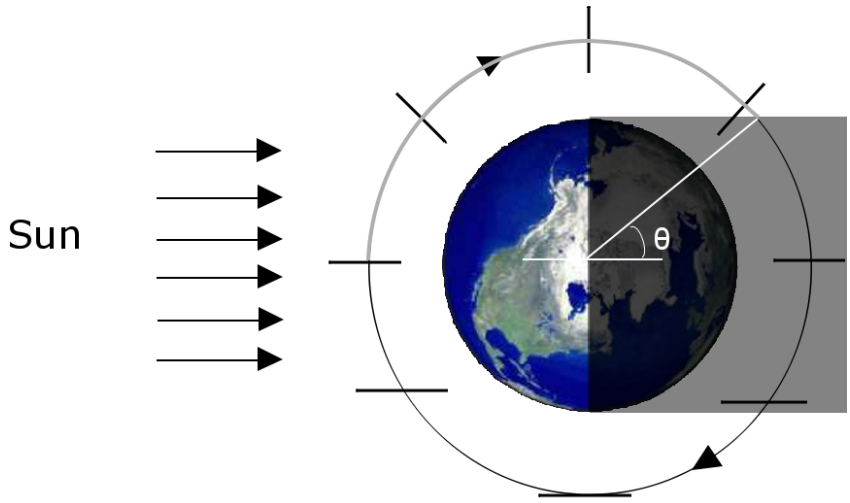

Figure 25 Solar sail de-orbiting

The satellite will orient itself so that the sail is perpendicular to the velocity direction if it is flying away from the sun, and when it is flying towards the sun it will align itself with the direction of incoming sunlight so that little or no force is imparted on the sail.

The part of the orbit during which the solar force will propel the satellite is indicated in gray. The angle of the orbit during which the solar force is present is given by 180° - θ, with

$$\sin\theta = \frac{R_e}{r} \qquad 39$$

With R_e the radius of the Earth and r the radius of the satellite orbit. For geostationary orbits this gives an angle θ of 8.7°. The angle that the sun makes with the sail also influences the force, as (from equation 7)

$$F_{normal} \approx F\cos^2 \propto \quad (40)$$

$$F = PA$$

Where F_{normal} is the effective solar force, F is the force that would have been imparted on the sail had it been facing the sun directly and α is the angle between the sail normal vector and the sun vector. P is the nominal solar radiation pressure at 1AU (4.5 x 10^{-6} Nm^{-2}) and A is the area of the sail. The above equation assumes that all photons are specularly reflected so that the tangential component is zero.

As a first attempt to calculate the required sail size for an end-of-life manoeuvre in GEO, consider the impulse resulting from one orbit.

$$I_{orbit} = \frac{T}{2\pi}\int_{-\frac{\pi}{2}}^{\frac{\pi}{2}-\theta} F\cos^2(\nu)d\nu = \frac{TF}{2\pi}\left[\frac{\nu}{2} + \frac{\sin\nu\cos\nu}{2}\right]_{-\frac{\pi}{2}}^{\frac{\pi}{2}-\theta} \quad (41)$$

Where T is the orbital period. This results in an impulse of I_{orbit} = 21500F for GEO, and consequently a ΔV of

$$\Delta V = 21500\frac{PA}{m} \quad (42)$$

per orbit.

A satellite in geostationary orbit has a velocity of 3.075 km/s. A satellite in a circular orbit 300km higher than this would have a velocity of 3.065km/s, resulting in a total ΔV of 10 m/s for the manoeuvre.

The time to perform the entire manoeuvre can then be found by finding the number of orbits required

$$n = \frac{\Delta V_{total}}{\Delta V} = \frac{\Delta V_{total} m}{21500PA} \quad (43)$$

In the above it is assumed that the orbital period does not change much. The orbital period at GEO is 1435 minutes and at the higher 300km orbit, 1451 minutes. For this first order approximation it is assumed that the period remains constant.

The total time to perform the manoeuvre is then n times the orbital period.

This produces the following graph for de-orbit times based on solar radiation pressure for a 1000 kg, 2000 kg and 4000 kg satellite at GEO.

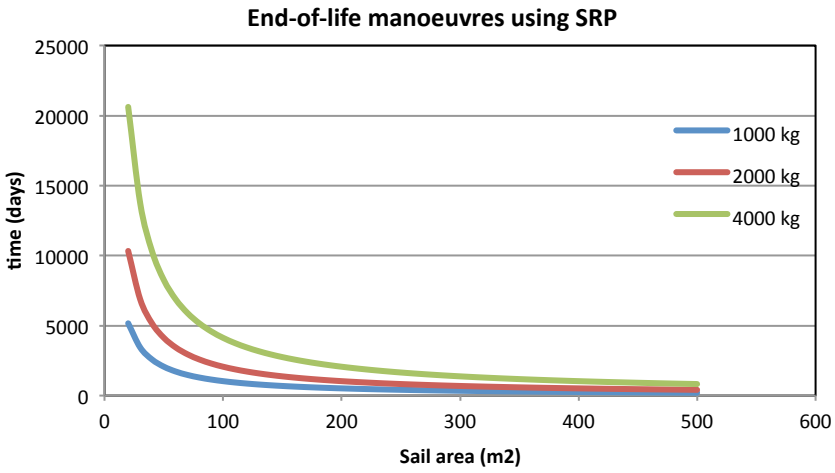

Figure 26 First-order de-orbit times for solar sail de-orbiting in GEO

From the graph it can be seen that a 50m^2 sail is sufficient to de-orbit even a 4000 kg satellite in the 25 year constraint using SRP.

Because of the non-symmetric application of the solar force, the orbit of the satellite will become more elliptical. A simple simulation shows this effect. The graphs below were obtained by numeric integration (Cowell integration). An exaggerated solar force was used together with an accurate sun model and Earth occlusion model.

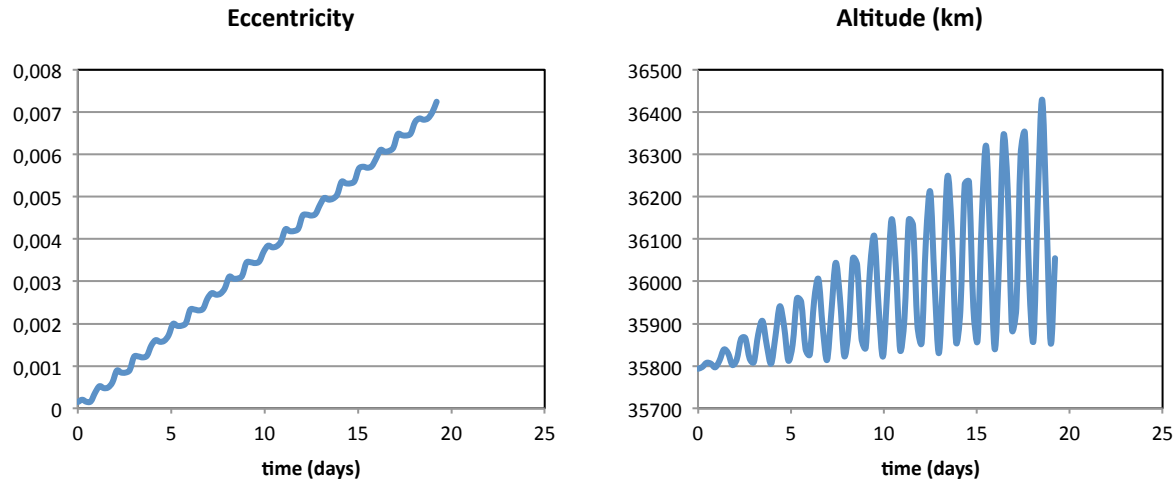

Figure 27 Increased orbital eccentricity in GEO de-orbit manoeuvre

The fact that the orbit eccentricity increases implies that the final de-orbiting time will be larger than the first order calculation. Also, the simulation above and the first order calculation does not take into account SRP resulting from the spacecraft body itself.

The same Cowell simulation was repeated for 3 test cases. The table below gives initial results for performing end-of-life manoeuvres for a GEO satellite with a mass of 1000kg.

Table 4-7 GEO solar sail de-orbit times

Sail size	Time to perform manoeuvre
5m x 5m	2350 days
10m x 10m	639 days
20m x 20m	236 days

One problem with the above approach is that the GEO belt is densely populated with each satellite in the region assigned a very specific longitude slot. The manoeuvre proposed above will cause the satellite with the sail to drift into neighbouring slots with a risk of colliding with other active satellites. In practise a larger impulse acceleration is required to ensure that a de-orbit manoeuvre does not intersect other satellite trajectories.

4.6 Conclusion

The different parameters that affect de-orbiting times have been analysed for both drag sails and electrostatic tethers. A graph (Figure 17) provides a look-up technique to determine required sail size for a given satellite (orbit and mass). It was found that increased solar activity leads to quicker de-orbit times, but that for long satellite lifetimes (>20 years) the epoch at start of de-orbiting becomes less relevant. We have also shown that elliptic orbits become more circular as a result of atmospheric drag.

The use of electrostatic tethers increases the maximum altitude at which the concept is feasible. For lower altitudes (<900 km), the quicker de-orbit time that can be gained is not worth the added complexity of the deployable tethers. The combined system with tethers is feasible for the altitude range 900 - 1300km (given a 25 year de-orbit constraint).

It is possible to use solar radiation pressure on a sail in the absence of drag to perform orbit manoeuvres. A complete investigation into this technique is outside the scope of this study.

Larger surface areas result in a larger total collision probability. The ideal sail size is the smallest size possible to de-orbit within 25 years. Information about the size of orbiting debris pieces is required to refine collision results.

5 HybridSail design

For HybridSail to be efficient as a de-orbiting device it needs to be as light as possible. Less mass means lower ballistic coefficient, higher characteristic acceleration and lower launch costs. With this in mind this section describes the design of a highly compact and small mass square sail with electrodynamic tethers.

5.1 Sail design

A rigid square sail was chosen for hybrid sail. The selection of a rigid structure is an obvious one as this will simplify the attitude control scheme by enabling passive attitude control and will maintain maximum drag area while it is subjected to aerodynamic drag. Provision is taken for the sail to utilise solar radiation pressure in order to decrease the de-orbit time. This is achieved by using a reflective membrane.

5.2 Booms

A rigid structure is formed by 4 booms or masts. There are many deployable boom technologies for large space structures. These include: wire deployers, telescopic booms, articulated masts, coil-able mast, inflatable booms and tubular booms.

Wire deployers such as yo-yo de-spin systems are commonly used to slow down the spin rate of a satellite. And they were recently utilized in the first and only successful solar sail mission to date, IKAROS, to deploy and tension its 20x20m sail.

Telescopic booms are usually used in applications requiring high strength, stiffness and retraction capability. However, given their current large mass-to-length ratio and deployed-to-stored size ratio compared to other boom options, to date, they have not been considered for gossamer spacecraft applications.

Coil-able masts are stowed by coiling the continuous structural members that run along the full length of the mast (longerons), into a tight helix hold inside a cylindrical canister. Once deployed, battens and diagonals provide additional structural support forming a truss structure. They can be stowed in less than 2% of their deployed length, and the shock load that occurs at full deployment, can be minimized using a lanyard running down the centre of the mast connected to a brake mechanisms or a motor driven drum. AEC-ABLE Engineering has developed coil-able masts with mass-to-length ratios of less than 50g/m, making them ideal for space deployable structures. The SAILMAST was used on NASA's 20x20m ground-demonstration mission.

Articulated masts are similar to coil-able masts, as they both deploy to form a truss structure. They allow more freedom in choosing the longeron material and cross section as they are stored by folding the longerons at pivot joint/articulations instead of by elastic deformation. Nevertheless, they have worst package ratios and are usually heavier than coil-able masts for similar mechanical property booms, due to their articulated joints.

Inflatable technology has been widely researched because it offers the lightest solution possible for large space structures. Current focus on inflatable booms have used an inflation system that will provide an internal pressure which will sustain the structural load until the external boom composite membrane is rigidized by ultraviolet or infrared radiation. However, this technology is still under examination to reduce leak issues and the risk of micro-meteorites puncturing the membrane before it is completely hardened. L'Garde has developed an iso-grid inflatable boom, which was tested in a 20x20m sail prototype, for NASA's future solar sail missions.

Tubular booms are flexible shells of different cross-sections that can be flattened and rolled-up onto a reel, like a carpenter's tape-measure. They obtain their stiffness during deployment by transitioning from a flat to a curved geometry. These booms are usually motor-driven or have a brake/speed-damper mechanism, rather than self-deployed, so as to control the deployment speed. The Storable Tubular Extendible Members (STEM) family of open-section booms, and their variations such as the Bi-STEM or the Interlocked Bi-STEM, are the most widely used type of deployable structure in space. Lenticular shaped (close-section) booms like DLR's and the Collapsible Tubular Member (CTM) were invented to increase the structural properties and reduce the height of the open-section tubular booms. Recently, the USA Air Force Research Laboratory (AFRL) has developed a tubular open-section boom called Triangular Rollable And Collapsible (TRAC) boom, consisting of

tape-springs welded back-to-back to form a triangular shaped structure. A metallic version of them were first used on NASA's NanoSail-D nano-solar sail, and are currently being considered for the LightSail-1 solar sail mission, and a CFRP version for the FURL sail.

Currently at the University of Surrey two different boom technologies are being developed as part of the CubeSail mission that would be ideal for HybridSail. These are summarised below.

A novel set of metallic booms was created from commercially-available measuring tapes. The tape-springs coating was stripped off and pairs of them were held front-to-front using Kapton tape so as to create lenticular shaped structures. The result is a boom that has a much higher bending and torsional stiffness than a single tape, while keeping its inherent ability to elastically coil around a drum. Also, the fact that the two tapes do not have welded areas and are therefore able to slide during coiling significantly reduces the shear stresses generated and the boom can be stored into a smaller volumes.

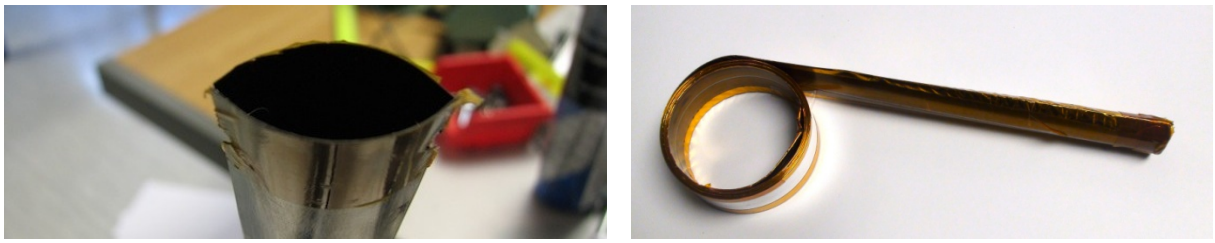

Figure 28 1.3m lenticular shaped metallic boom with Kapton tape coating

These booms use the elastic strain energy of the coiled state to self-extend once the constraint mechanism releases them. They are guided out linearly through openings on walls of the booms deployment module. The figure below shows the time-lapsed sequence of a successful deployment of the 1.7x1.7m prototype model and its angular (roll) rates. A similar test has been carried out placing the system on an air-bearing table to asses these rates in a more realistic manner. As can be observed from the figure, due to the high strain energy of the metallic booms the sail unfurls very quickly, which is of special concern as fairly high shock loads are generated once the booms fully extend. A passive speed-damper mechanism that acts as a brake for the booms spindle is currently under consideration to tackle this issue.

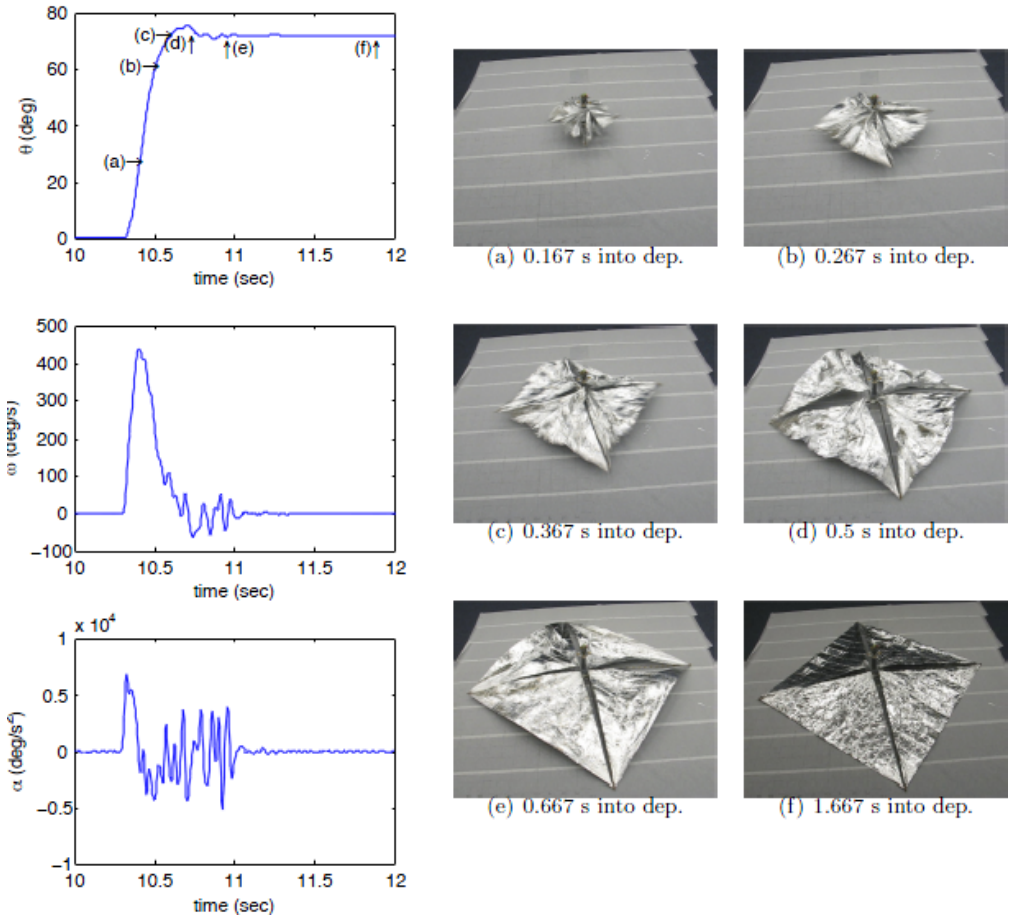

Figure 29 Deployment sequence of the 1.7x1.7m 4-quadrant sail prototype with metallic booms

Besides this, since the coiled configuration is in an unstable high-energy state, the booms tend to blossom when stored and during deployment. This was found, through the multiple deployment tests carried out with the early engineering model where the booms got jammed on some occasions. Therefore, an anti-blossoming mechanism that produces a force normal to the direction of the booms extension is also required. Additionally, in order to save mass, each boom is planned to be guided out linearly through two low-friction Delrin rollers, and thus completely eliminating the walls of the deployment module.

Currently an improved engineering model with all of the above mentioned changes and the use of space-rated materials is being produced. For this, Beryllium-Copper was chosen as the material for the booms given its long space-heritage, non-magnetic characteristic and optimal mechanical properties. A manufacturing facility has been set up at the University of Surrey to produce in-house BeCu tape-springs with different curvatures. Also a custom-made aluminized Kapton tube (sheath) has been ordered to coat the booms and provide thermal stability. The latter was decided in order to avoid the inevitable outgassing problems of the Kapton tape´s glue in the vacuum of space.

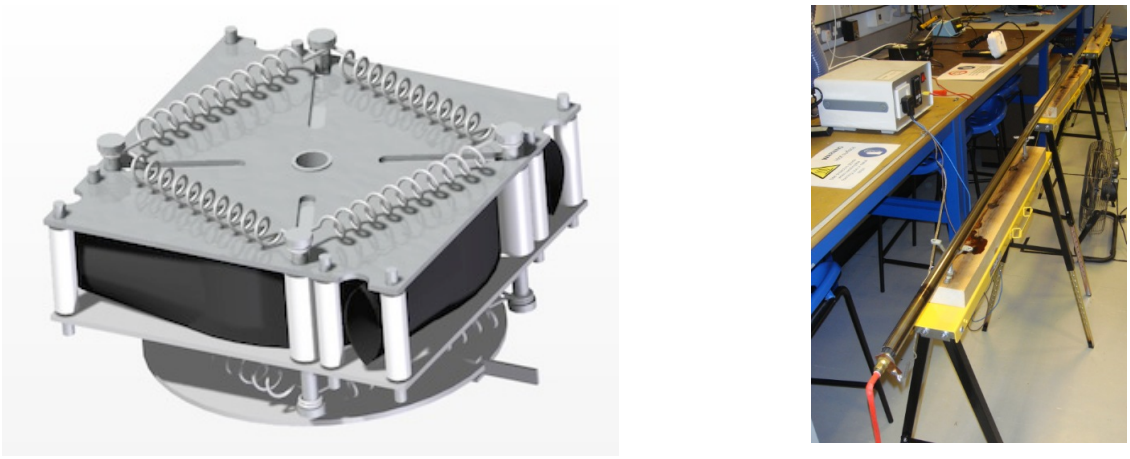

Figure 30 New Surrey boom deployment mechanism CAD drawing (left) and metallic booms manufacturing facility set-up (right)

The second proof-of-concept prototype for the sail deployment system was produced as an alternative to overcome some of the inherent issues of using large flexible metallic structures in orbit. The reliability of this second concept is a result of using bi-stable reeled composite (BRC) booms. The booms have essentially the same geometry as a standard STEM or tape-spring, but where these only have a single stable state (extended), the BRC booms have a second stable configuration (coiled). This second strain energy minimum entails that they do not want to blossom when rolled-up or spontaneously jump to the zero energy state through an unpredictable 3D motion.

A novel change was introduced in the composite lay-up to produce structures that are now bi-stable over the whole length. Previously, BRC tubes enabled relatively small final-to-initial coiling diameter ratios in order to keep the bi-stable effect. This change then resolves the previous length restriction of these structures, making them scalable to very long lengths. Also, the discovery produces a boom that wants to deploy in a very controlled and coherent manner by unravelling itself around the drum while the rest of the boom is still coiled up. Therefore, the deployment mechanism utilized in this concept is significantly simpler, resulting in a very light design that reduces failure modes.

For small versions of hybrid sail up to 5m x 5m the metallic concept is ideal due to its low manufacturing costs. As the sail size increases the use of the metallic booms becomes less favourable due to its large mass. So the BRC concept is suitable for large versions of HybridSail.

5.3 Sail membrane and folding

Membranes used for sails are usually light and preferably highly reflective to take advantage of the solar radiation pressure. Some of these are the CP-1 polyimide developed by NASA and the Aluminized Kapton Film or Mylar Film. A sail's effectiveness as a deorbiting mechanism during Drag-Sail mode is realized by increasing the area of interaction with air particles.

The presence of micrometeorites and small debris particles in low earth orbit will result in a mean incidence of particles less than 0.1mm at 800km, a particle every 2.3 days. Thicker Kapton membranes (which have high tensile strength, good bulk density and good UV life) can be used. The structure of the membrane can be reinforced with a net pattern so as to minimize tear.

A number of different folding and suspension techniques have been tested as part of the CubeSail mission. It has been found that for booms which extend linearly during deployment such as the metallic boom concept a four quadrant sail folded using Z-folds in an accordion-like manner, with the fold lines perpendicular to the hypotenuse of the triangles yields the best results. As the crease lines are at large angles with respect to the tension lines coming from the sail corners, the membrane is fully taut when the booms are extended out.

As indicated previously there is a real risk of tearing of the sail even if rip stop techniques are used to minimise the propagation of rips. Since the sail is attached to the boom in only three points any tear near them can cause the whole quadrant to be lost. To prevent this from occurring a completely stripped sail concept is utilized. This consists of dividing the whole film into strips of sail. The loss of one or several strips due to rip propagations has a smaller impact on overall performance when compared to simply supported sails. Furthermore this enables a low-stress state in the membrane with less structural mass requirements for the supporting booms due to the fact the each strip is attached along the boom length. This method though cannot be implemented with linearly extending booms, only with the BRC concept which deploys in a circular fashion.

5.4 Sail shape

For best aerodynamic passive stability the sail should have a shuttlecock/cone shape. This conical shape moves the centre of pressure (CP) behind the centre of mass (CM). Any misalignment of the centre-of-mass, centre-of-pressure and the velocity vector will cause a restoring torque to realign them. This way HybridSail will be passively stable while in drag mode for the largest portion of its operation life.

Harkness , [25], through a number of simulations has shown that for a cone shaped drag augmentation device the optimal apex half angle for an initial altitude of 450km is 1.55 radian and for 650km 1.4 radians.

5.5 Electrodynamic tethers

Electrodynamic tethers are a form of propulsion that utilises the solar wind as a thrust force. It essentially consists of long positively or negatively charged conductive tethers. The solar wind ions are repelled by the charged tethers and momentum is extracted. The solar wind dynamic pressure is about 5000 times weaker than the solar radiation pressure. This fact though does not pose an impassable obstacle. The effective interaction area of an electric sail is not a physical one but a virtual one. The ions can interact with the tethers from a distance of about 100m depending on the charge of the wire thus creating a very large effective interaction area.

Due to charge built up an electric sail needs a way to discharge so it can maintain the large potential required for ion interaction. This can be achieved by using an electron gun if the tethers are positively charged or an ion gun for negatively charged tethers. Both types of discharge devices will add significant mass and have very high power requirements in the context of HybridSail design. Furthermore ion guns require the need of a propellant from which ions will be formed. These factors make it a non ideal solution for HybridSail both due to the mass and the fact that power generation will be required for the operation life of the tethers.

Many attempts have been made to deploy long tethers many of which have not been successful adding one more layer of complexity to the already complex sail deployment. Due to the presence

of micrometeorites and other space debris the tethers need to be resilient to impacts and provide multiline redundancy such as the Hoytether [26].

In order to provide usable thrust, tethers need to be long as seen from the simulations ranging from 400m to 6400m depending on the mass of the object to be de-orbited. Furthermore the initial part of the tether needs to be insulated longer than the Debeye length so that the emitted electrons and ions are not attracted back to the tethers. Multiple tethers in a spin stabilised nature as shown in the figure below cannot be used. The spin required to keep the lines taught will cause gyroscopic stiffness to the system causing HybridSail to be inertially fixed. This way the drag-sail will not be effective since for a portion the orbit the drag force will be in-line with the velocity vector and the other portion be opposite and cancel each other. So both modes of operation cannot work concurrently. The tethers need to be deployed first for high orbits and then cut away for the drag mode to be operational. The only way to have both modes operational at the same time is to have one long tether as shown below.

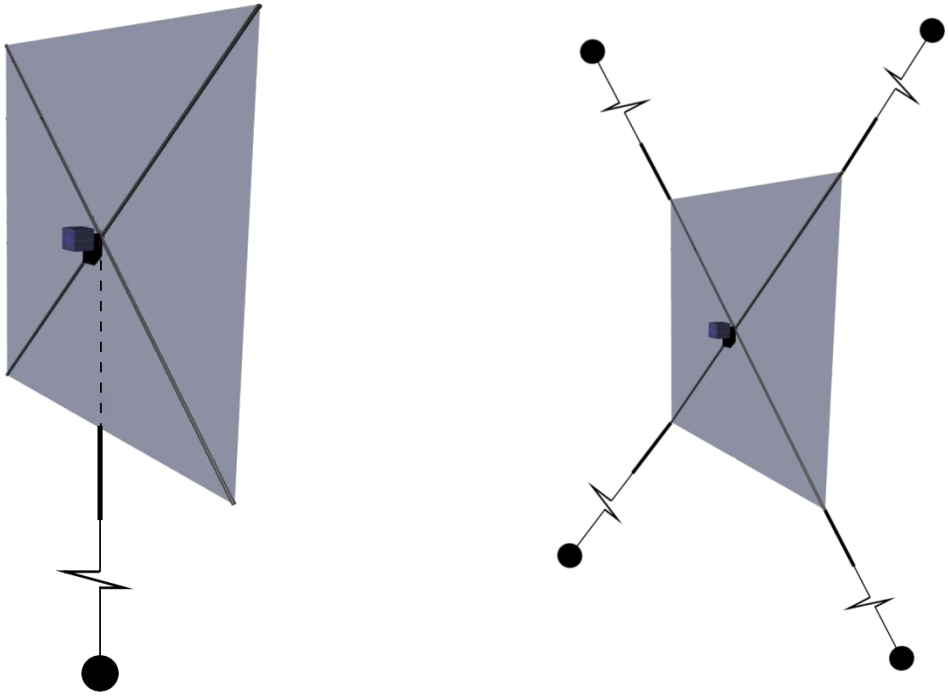

Figure 31 Single tether (left) and multiple tethers in spin stabilized configuration (right)

5.6 Conclusions

Tethers have a number of issues that make them unfavourable:

- Low Technological Readiness Level
- Problems with the long tethers
- Difficulty in attitude control
- Large added mass
- Constant power requirements
- Low added force

- Higher Risk

Based on the reasons stated above it can be concluded that to the best way to create an efficient low cost de-orbiting device is to only utilise the sail as a drag augmentation device along with solar radiation pressure for higher altitudes.

By using only a sail the system can be simplified with only the sail deployment having a higher risk. Since the sail will have pyramidal shape, passive attitude control can be utilised. This way it becomes much more reliable and power/working electronics will not be required for the longest part of the sails operational life. When the sail works in solar sail mode magnetorquers can be used to provide the necessary attitude control torques.

6 Docking system design

A number of different methods have been suggested in the past for docking with satellites and other space debris. In this section some of these methods are discussed and evaluated both as to their usability with respect to the HybridSail concept but also in general as a concept. At the end of this section a comparison table is provided for all the proposed solutions.

6.1 Nets

Nets have been proposed many times in the past due to their ability to collect large debris and simplicity. A large spinning net with a number of small weights at the tips is ejected from the capturing satellite which is attached by a tether. Due to the spin, the small end weights open the net and keep it open until contact. Once the net makes contact the natural motion of the weights will cause the net to close and engulf the debris. This way large pieces of debris can be captured.

In 1990 SPECS Inc. of the University of Texas at Austin [27] conducted a study for the removal space debris. Their selected capture mechanism was a net. The net was to be fired from spring loaded launch tubes with spiral grooves to cause the net to spin at a rate of 1.6 revolutions per second with a velocity of 1.1m/s which would cause the net to open 1 meter after ejection. A tether connects the net with the launch tube. The net would be closed by a mechanical pulley that gets activated when the tether reaches its end or when a collision is detected by a small accelerometer on the net. After the successful capture the net would be reeled back in to the launch tube to secure the debris. This means debris with a small diameter can be captured since the launch tube needs to be as big as the debris itself.

Astrium as part of the ESA Robotic Geostationary orbit Restorer (ROGER) [28] study chose a net as well to capture satellites in geostationary orbits. Roger would have 20 throw-nets with each net mechanism having a mass of 9kg with 4 or 6 weights at the tips to open the net each being 200g. The nets would be ejected with a final velocity of 1m/s by a spring system. Two net sizes were proposed one 10mx10m and 15mx15m with a mesh of 40cm. A 50m long cable with a diameter of 2mm was used.

Beihang University [29] also has suggested the use of nets for capturing. The image below demonstrates the ROGER concept [28].

Figure 32 Astrium ROGER net capture device

The volume requirements of the net itself are minimal and can be easily scaled for mission requirements. Since a net can only be ejected once the capturing satellite will need more than one net for redundancy in the case the first net misses the target. This redundancy offsets the advantages offered in volume and mass for the case of the hybrid sail. Another disadvantage of this method when used with the hybrid sail concept is that due to the ejection of the net and the small size of the bus the bus will be significantly accelerated away from the debris. When a net is used with a non cooperative, tumbling piece of debris, the dynamic behaviour of the system will be very difficult to predict and might result in damage to the capturing satellite. Furthermore because the captured debris is not held firmly, the magnetorquers cannot be used to dump any rates that might be present. For these reasons even though the net can be used for larger platforms it is not suitable to be used by the hybrid sail concept.

6.2 Robotic arms

The other family of proposed methods make use of an articulated robotic arm. A stowed arm with multiple joints is extended using deployable booms with an end-effector to firmly grasp the debris.

As part of the previously mention ROGER study QinetiQ [30] suggested the use of several rigid and articulated or semi-rigid tentacles to encircle the body of the target as shown below. Their capture mechanism was dubbed the “octopus tentacle solution”. It consists of a segmented tubular telescopic boom with whose segments are locked to make the joints stiff. The final segment which supports the tentacles is not lock but is spring loaded and allowed to be pushed back to guarantee a soft contact with the target object. Four tentacles with a soft contact surface are used which can be controlled independently or simultaneously. The tentacle joints are spring loaded to a normally closed position. Shape memory alloy wires are used to provide the opening torque.

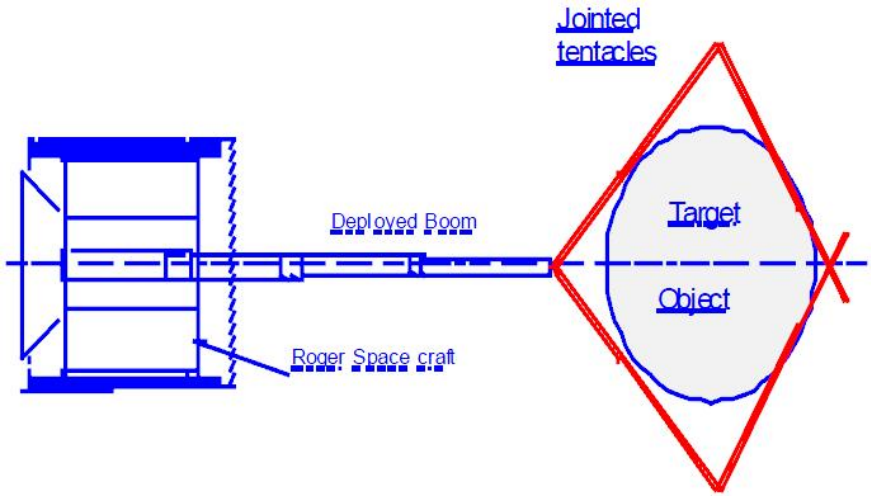

Figure 33 QinetiQ octopus tentacle solution [30]

The Japan Aerospace Exploration Agency (JAXA) has also considered the use of robotic arms for the capture of debris [31, 32]. Their solution though has some differences form the QinetiQ one. Instead of using a rigid segmented telescopic tubular boom they use an extensible flexible boom. The flexibility of the boom is used to buffer and break any residual motion of a non cooperative satellite. They have also developed and simulated a joint compliance control algorithm for controlling the joints of the arm.

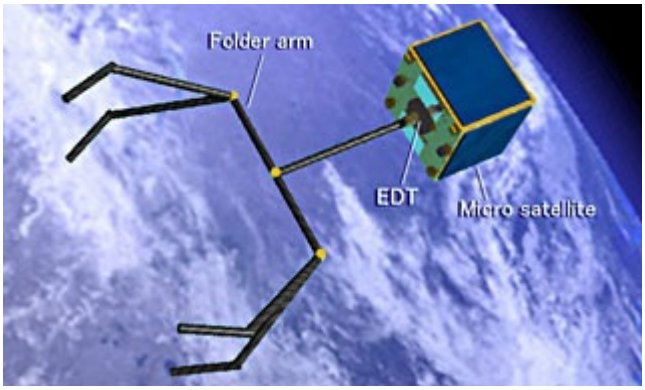

Figure 34 JAXA Folder arm [32]

Cranfield University has carried a study on orbit debris removal called DR LEO [33], they have also opted for a robotic arm much different from the other two previously mentioned studies. They proposed the use of a more conventional robotic arm with 6 degrees of freedom linked by 3 rods leading to an end-effector. In contrast with the other studies that use long arms to encircle the

whole debris their end-effector is a clamp using a high power DC motor to grasp at the edge of the nozzle of an Ariane 4 upper stage.

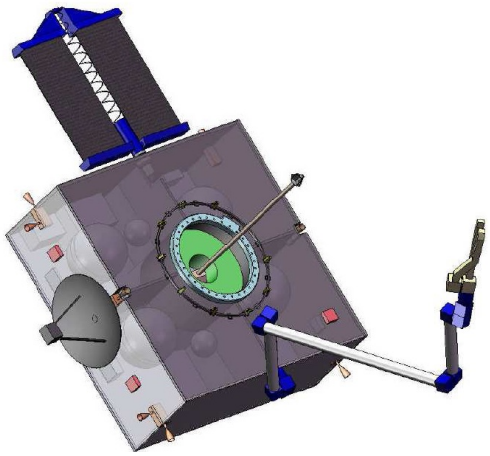

Figure 35 Cranfield University DR LEO robotic arm [33]

Some other robotic arm concepts are pictured below.

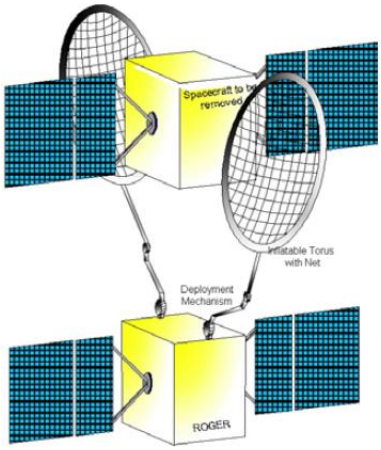

Figure 36 QinetiQ netted inflatable torus

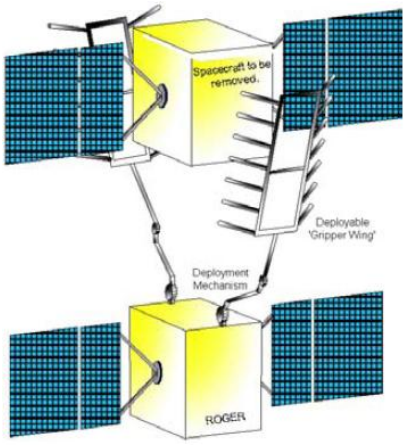

Figure 37 QinetiQ mechanical rakes [30]

If a clamp end-effector is used, almost any debris of any size can be captured. The cone adaptor of any size satellite can be captured offering greater flexibility. The autonomous targeting of a single point on a non cooperative debris can be a daunting, almost impossible task requiring computationally intensive image analysis. Furthermore a host spacecraft with high agility is required to navigate and maintain a stable position close to the target object. Very precise control is required both for the attitude and the robotic arm in order to avoid unwanted collisions between the two spacecraft. The tentacle robotic arm solutions require a spacecraft with lower capabilities. The flexible boom will damp some of the vibration when capturing a non-cooperative debris. Because the tentacles are large enough to enclose the whole debris they can be closed in a controlled manner so as to remove small initial tumbling rates although are not capable grapping objects with high tumbling rates. Furthermore brushes can be used to damp some of the rates. The nature of these tentacle systems though requires prior knowledge of the size debris in order for it to have the correct dimensions. Robotic arms can carry multiple capture attempts unlike nets. The physical size, mass, platform capability requirements make robotic arms unsuitable for use with the hybrid sail concept.

6.3 Tethers Unlimited Inc (TUI) The Grasp technology

The TUI GRASP (Grapple, Retrieve, And Secure Payload) solution [34] offers some advantages over nets: primarily the fact the it's not a single attempt solution. It uses lightweight inflatable booms to deploy a large net structure to capture an object. This solution is lightweight and simple and can be carried by nano-satellites. A 3-U CubeSat GRASP prototype has been successfully tested in a microgravity environment.

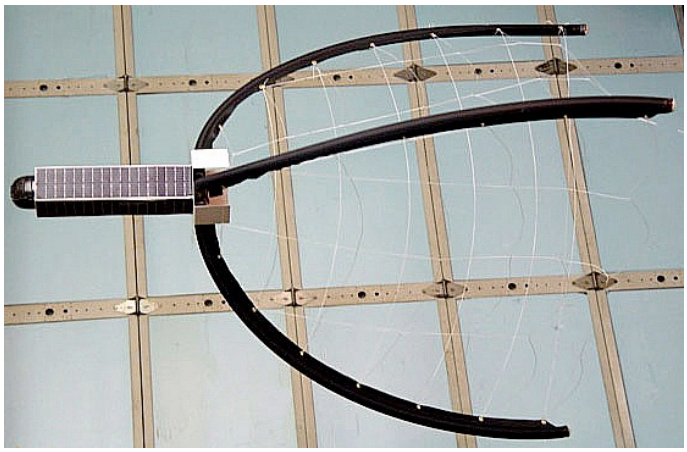

Figure 38 TUI's GRASP technology [34]

6.4 Grabber

A concept currently being investigated at the University of Surrey is to use a mechanical grabber to firmly attach to the target debris. It essentially consists of a spring loaded claw with enough force to puncture the first layer of the satellite and imbed itself in the honeycomb structure. This way any debris of any size can be captured without the need of prior knowledge of its dimensions.

The spring loaded claw is fired from the HybridSail bus and attached to it by a tether. Upon contact the claws close and puncture the shell of the satellite. For optimal performance a corner of the satellite needs to be targeted, requiring extensive image analysis and calculation. Also the platform needs to be very stable. In case the claw misses its target it can be reeled in and fired again making it reusable. When the claw has successfully captured the debri it will reel it in for a firm connection with the hybridsail bus. This will enable magnetic detumbling and greatly ease the attitude control

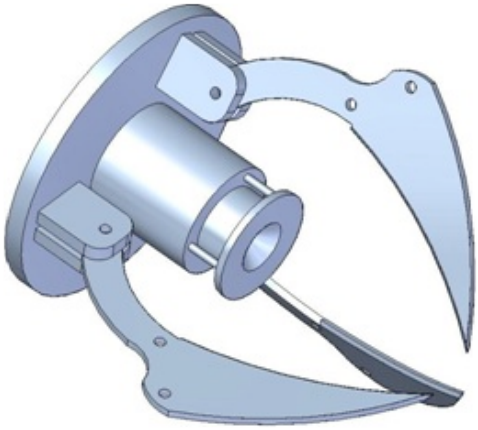

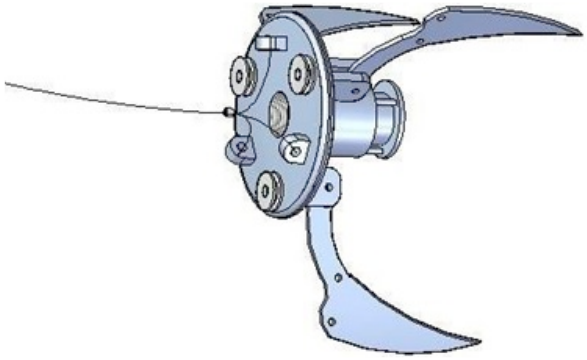

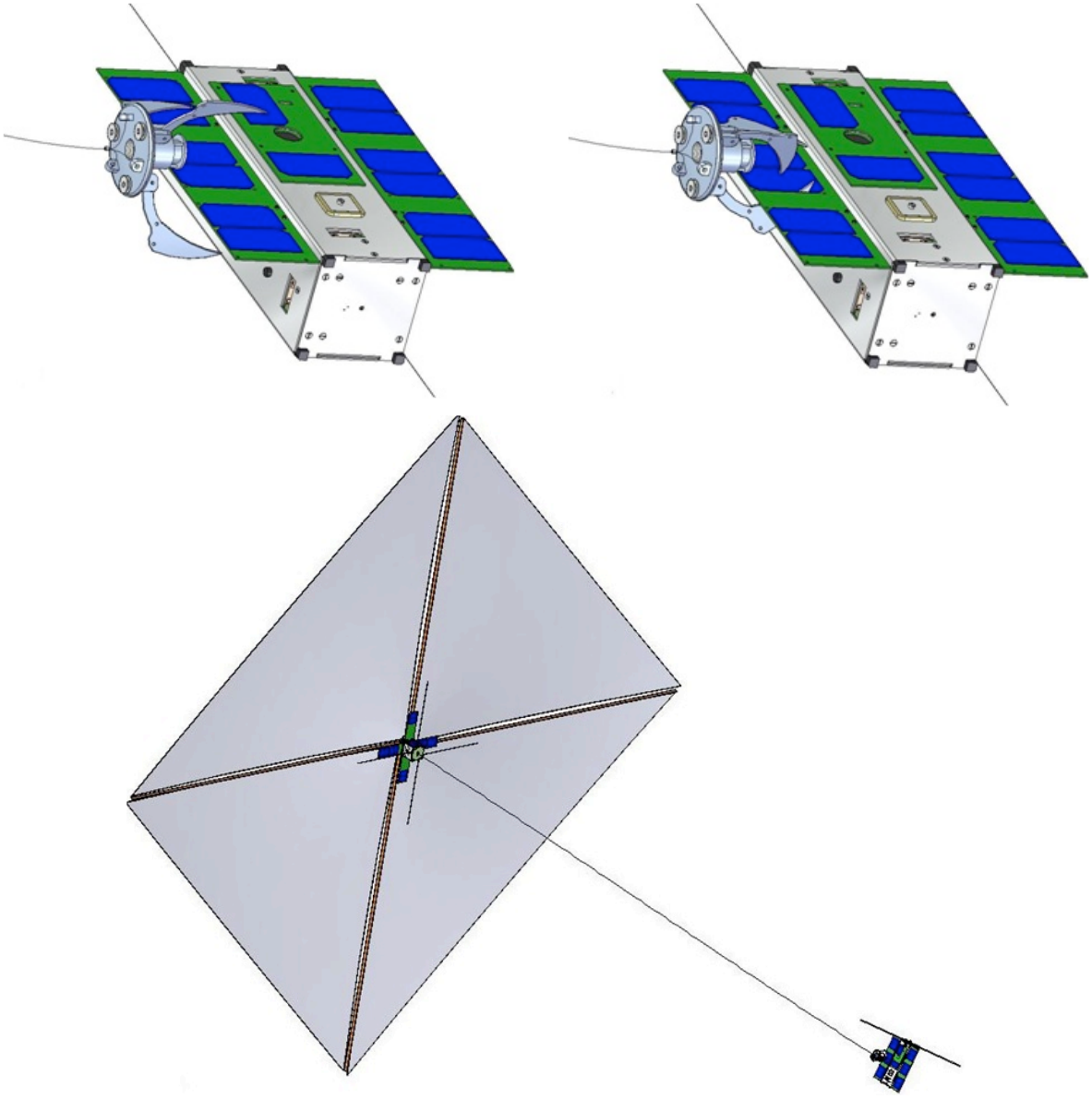

Figure 39 SSC Grabber

6.5 Comparison/Conclusion

The various technology options for docking with debris are evaluated in the table below. Per category each option is evaluated for how well it satisfies the category. A number ranging from 1 to 5 is assigned to each option depending with 1 being the most favourable.

	Nets	Robotic Arms/ Tentacles	Robotic arms/ Clamp	TUI GRASP	SSC Grabber
Mass	2	4	4	2	2
Volume	1	4	3	2	2
Platform Demand	1	4	5	2	3
Reusability	5	1	1	3	1
Cost	2	5	5	2	2
TRL	4	3	3	2	3
Sum	15	21	21	13	13

Based on the above table it can easily be concluded that the best solution is offered by the TUI GRASP technology.

7 Attitude Control

As shown in Figure 13 drag de-orbiting requires that the sail rotates as the satellite moves in its orbit so that the sail is always perpendicular to the velocity vector. This requires a stable roll, pitch and yaw angle and can be achieved by active attitude control or other passive means. The hybrid sail-tether concept discussed in this study would require a more complicated attitude control system, because not only does the sail orientation have to be controlled, the satellite also would have to spin about the x-axis to keep the tethers taut. The spinning motion would introduce gyroscopic stiffness, making the pitch rotation more complicated. The design of such a control system is beyond the scope of this study.

For the attitude control portion of HybridSail we have focussed on 2 concepts. De-tumbling of an uncooperative debris piece using small magnetic actuators only, and passive stabilization of the sail using a shuttlecock design.

7.1 De-tumbling using magnetic control

This section shows the feasibility and benefits of the use of magnetic control to detumble large space debris with a docked ADCS system. This section assumes that the intercepting HybridSail satellite has already docked with a debris piece and that the debris and docked satellite can be modelled as the same rigid object with the moment of inertia of the larger object. It is further assumed that the sail and/or tethers have not been deployed yet. The ADCS system will make use of magnetic torquer rods to de-tumble the combined mass.

The time span for the de-tumbling can be relatively large so that small torque rods can be used, resulting in a small ADCS sub-system. The block diagram for the magnetic de-tumbling ADCS is shown below.

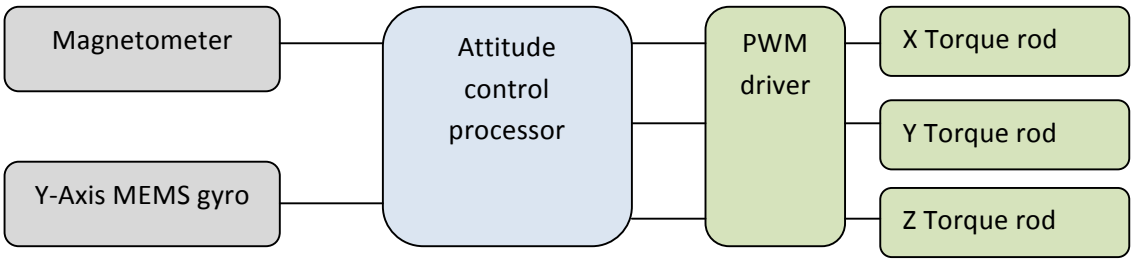

Figure 40 De-tumbling ADCS block diagram

7.1.1 De-tumbling controller

A combined B-dot [23] and Y-Thomson [24] controller is used for de-tumbing. This will reduce the angular rates around the X and Z axes to zero while maintaining a reference rotation rate about the Y-axis. The torquer commands generated by the controller are given by [13]:

$$M_y = K_d \frac{d\beta}{dt} \quad (44)$$

$$M_x = K_s(\omega_{yi} - \omega_{yref})\text{sgn}(B_{mz}) \text{ for } |B_{mz}| > |B_{mx}|$$

$$M_z = -K_s(\omega_{yi} - \omega_{yref})\text{sgn}(B_{mx}) \text{ for } |B_{mx}| > |B_{mz}|$$

Where

$$\beta = \cos^{-1}\left(\frac{B_{my}}{|\mathbf{B}_{meas}|}\right) \quad (45)$$

Is the angle between the body Y axis and local magnetic field vector, K_d and K_s are the de-tumbling and spin controller gains, ω_{yref} is the reference Y body spin rate and $\mathbf{B}_{meas} = [B_{mx} \quad B_{mx} \quad B_{mz}]^T$ is the magnetometer measured magnetic field vector in satellite body coordinates. ω_{yi} is the inertially referenced Y-angular rate. It is common practise to obtain estimated angular rates from Kalman filtering of magnetometer data, but in this case we will use a Y-axis aligned MEMS gyro for this measurement as in [13].

$\mathbf{M}_{PWM} = [M_x \quad M_y \quad M_z]^T$ is then the PWM (pulse width modulation) controlled magnetic moment vector of the torque rods. The pulse outputs are further saturated to 80% of the sampling period so that the residual magnetic moment can die away before the magnetometer is sampled. The elements of $\mathbf{M}_{PWM}$ are thus numbers ranging from -$0.8T_s$ to +$0.8T_s$ where T_s is the sampling period.

The average magnetic moment is then given by

$$\mathbf{M}_{avg} = \frac{M_{max}}{T_s}\mathbf{M}_{PWM} \quad (46)$$

where M_{max} is the maximum magnetic moment the torque rod can deliver. The resulting control torque is

$$\mathbf{N}_{MT} = \mathbf{M}_{avg} \times \mathbf{B}_b \quad (47)$$

Where $\mathbf{B}_b$ is the true magnetic field vector in satellite body coordinates.

7.1.2 Torquer sizing

The control torque generated by the rods must be large enough to overcome the disturbance torques that the satellite would encounter. They are: gravity gradient torque, aerodynamic drag and solar radiation pressure generated torque.

We limit the analysis to two cases: an upper stage of a Pegasus, Falcon or ICBM-class launch vehicle upper stage and an Ariane 5 upper stage.

	Pegasus, Falcon or ICBM upper stage	Ariane 5 upper stage
Moment of inertia	Diag(300, 600, 300)	Diag(8058, 11148, 6479)
Drag/SRP area	10 m^2	20 m^2

Using the parameters from the above table, we can determine the order of the disturbance torques for a given orbit altitude. The altitude affects the drag disturbance, but also the magnetic field magnitude decreases with altitude making the torque rods less able to overcome disturbances.

	Altitude	Pegasus, Falcon or ICBM upper stage	Ariane 5 upper stage
Gravity gradient	-	5.0×10^{-4} Nm	6×10^{-3} Nm
SRP torque	-	4.0×10^{-5} Nm	2.0×10^{-4} Nm
Aerodynamic torque	500 km	1.0×10^{-5} Nm	5.0×10^{-5} Nm
	800 km	3.0×10^{-7} Nm	8.0×10^{-7} Nm
	1200 km	5.0×10^{-8} Nm	1.5×10^{-7} Nm
Magnetic field magnitude	500 km	2.0×10^{-5} T to 5.0×10^{-5} T	
	800 km	2.0×10^{-5} T to 4.0×10^{-5} T	
	1200 km	1.5×10^{-5} T to 3.5×10^{-5} T	

It can be seen that the largest disturbance torque in both cases is due to gravity gradient. Using equation (47), this would suggest the following magnetorquer sizes to overcome the disturbance torque: For the Pegasus upper stage a maximum magnetic moment of 10 Am^2 is required and for the Ariane 5 upper stage 100 Am^2.

7.1.3 Results

The following figure shows the simulation of the de-tumbling of an upper stage of a Pegasus, Falcon or ICBM-class launch vehicle upper stage with the following parameters:

Physical parameters	
Moment of inertia	Diag(300, 600, 300)
Maximum magnetic moment	10 Am^2
Initial orbit	
Altitude	700 km
Eccentricity	0.001
Inclination	97.77 deg
Initial attitude	
Initial tumble rates	[0.2, -1.0, -0.3] deg/s

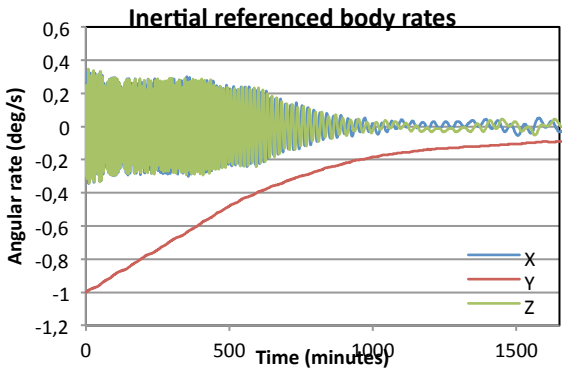

Figure 41 Detumbling Simulation of a Small Satellite Launch Vehicle Upper Stage

If we repeat the same scenario for the Ariane 5 upper stage with larger torquer rods, the following results are achieved:

Physical parameters	
Moment of inertia	Diag(8058, 11148, 6479)
Maximum magnetic moment	100 Am^2
Initial orbit	
Altitude	700 km
Eccentricity	0.001
Inclination	97.77 deg
Initial attitude	
Initial tumble rates	[0.2, -1.0, -0.3] deg/s

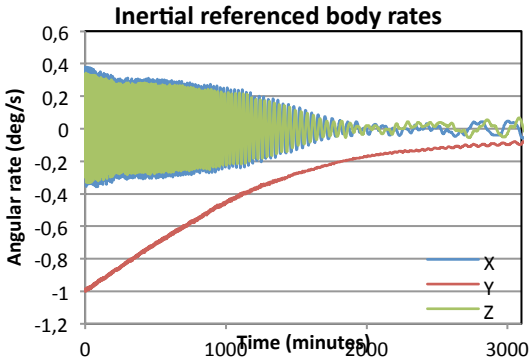

Figure 42 Detumbling Simulation of a Ariane 5 Launch Vehicle Upper Stage

In reality, the initial tumbling rates can be much higher in the above simulations. Rocket upper stages are sometimes intentionally accelerated to a high angular rotation at the end of their mission (> 45 deg/s). If we repeat the above simulations with initial tumbling rates 10 times larger than before, the following results are achieved:

Scenario	Time to de-tumble
Small Satellite Launch Vehicle Upper Stage	6.1 days
Ariane 5 Launch Vehicle Upper Stage	11.9 days

It can be seen that as long as the torque produced by the torque rods are large enough to overcome the disturbance torques, the satellite can be de-tumbled from any initial rate – it just takes longer.

7.2 Passive stabilisation due to sail shape

In this section we investigate making use of a specific sail shape to passively stabilize the satellite as a result of drag forces.

Having a passively stabilized sail has significant impact on the requirements for the rest of the system. An active control system requires a power system (batteries, solar panels etc) with the added mass and volume that these components contribute. On top of this, all of these components have to keep working for the remainder of the de-orbiting time, which can be as long as 25 years.

A passively stabilized sail removes the need for a control system and power supply, greatly reducing the complexity and saving on mass and volume.

The proposed sail configuration is shown in the diagram below. This is achieved by angling the booms out of the x/z plane.

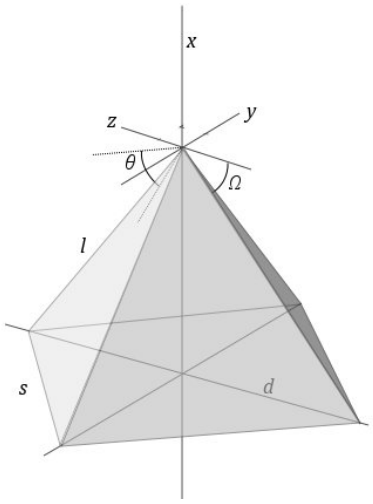

Figure 43 Sail design for passive stabilization

The resulting sail consists of 4 triangle segments in a pyramid shape. The angle between a boom and the x/z plane is Ω, while the angle between a sail segment and the x/z plane is θ. The relationship between the two angles is given by

$$\sqrt{2}\tan\theta = \tan\Omega \tag{48}$$

The length and height of the pyramid base is then given by

$$s = \sqrt{2}l\cos\Omega \tag{49}$$

And the height of the pyramid is

$$h = l\sin\Omega \tag{50}$$

Resulting in a segment area

$$A_{segment} = \frac{1}{2}s\sqrt{h^2 + \frac{s^2}{4}} \tag{51}$$

The cone-shaped sail does have a negative impact on the projected sail area and coefficient of drag. The resulting drag force will be smaller for the cone-shaped sail, resulting in a longer de-orbit time, compared to the same boom lengths in a flat configuration. The projected drag area of the cone-shaped sail is given by

$$A_{p,cone} = 2l^2\cos^2\Omega \tag{52}$$

The ratio of projected area for the cone-shaped sail versus a flat sail (with equal boom lengths) is thus

$$\frac{A_{p,cone}}{A_{p,flat}} = \cos^2\Omega \tag{53}$$

For a boom cone angle of 10 degrees (as suggested in [25]) the above ratio is 0.97.

The normal vector of each sail segment is given by

$$\mathbf{n}_i = \mathbf{R}_i[\sin\theta \quad -\cos\theta \quad 0]^T \tag{54}$$

Where i =1..4 and $\mathbf{R}_i$ is a rotation matrix that will rotate about the x-axis by angle $\alpha_i = \frac{\pi}{4} + \frac{i\pi}{2}$.

$$\mathbf{R}_i = \begin{bmatrix} 1 & 0 & 0 \\ 0 & \cos\alpha_i & -\sin\alpha_i \\ 0 & \sin\alpha_i & \cos\alpha_i \end{bmatrix} \tag{55}$$

The centre of pressure vector (relative to the top of the pyramid) of each sail segment is given by

$$\mathbf{c}_i = \mathbf{R}_i \left[-\frac{1}{\sqrt{2}}\cos\theta \sqrt{h^2 + \frac{s^2}{4}} \quad \frac{1}{\sqrt{2}}\sin\theta \sqrt{h^2 + \frac{s^2}{4}}\theta \quad 0 \right]^T \tag{56}$$

It is assumed that the centre-of-mass coincides with the top of the pyramid. We can now simulate the attitude dynamics of the cone shaped sail by propagating the attitude as described in section 3. The aerodynamic torques causes by the sail segments are calculated individually from equation (3) and then summed.

The orbit that was used for the simulation is circular with an altitude of 400km. An initial yaw angle of 30 degrees was selected with pitch and roll at zero. A sail angle, θ, of 20 degrees was used. The attitude angles are plotted below.

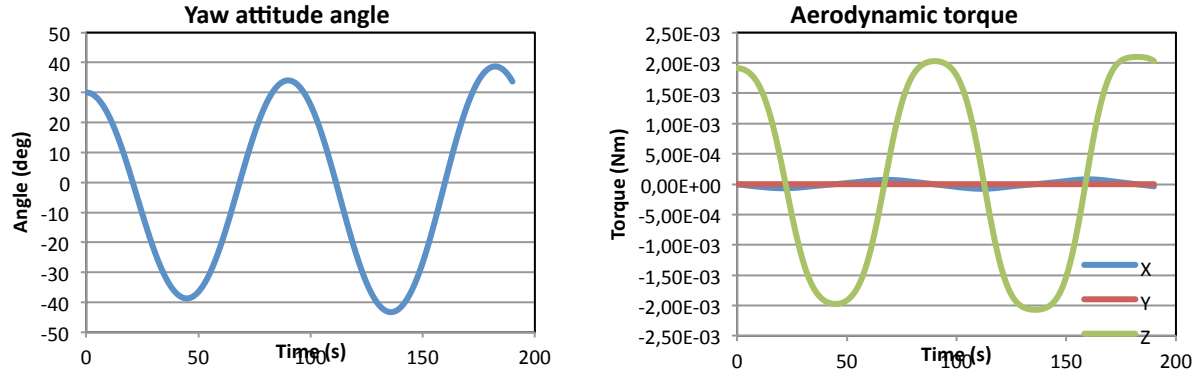

Figure 44 Attitude angles and aerodynamic torque of passively stable sail

It can be seen that the shaped sail results in a torque that will rotate about the z (yaw) axis to restore the sail yaw angle, but that the angular motion is not damped, resulting in an oscillation.

The oscillation can be removed by making the sail structure non-rigid. This would be achieved by having a flexible boom-base attachment, such that the booms can rotate out of plane, but spring loaded so that the booms will return to a zero out-of-plane angle when no force is present. This way, the structure will transform into the cone shape when the force on all 4 segments are equal, but segments experiencing smaller force will be closer aligned to the Y/Z plane, thereby damping the above mentioned oscillation. A further investigation of this effect is warranted.

8 Conclusions

In this study we have shown the feasibility and limitations of a docking and de-orbiting device based on a deployable sail and tethers that use aerodynamic drag and electrostatic forces to de-orbit. An efficient and accurate method was implemented to assess de-orbit time span under various test conditions.

We have presented an analysis of the de-orbit times achievable with such a concept and also the parameters that play a role in de-orbiting. We have also described the satellite and docking system concept design with a comparison with existing/proposed technologies. Lastly, we have presented 2 attitude control techniques relevant to the HybridSail concept.

The combined sail/tether concept poses an advantage in the fact that it can be used to de-orbit from higher altitudes than achievable with a drag sail alone. It was however found that tethers adds complexity to the satellite design and deployment, results in a larger mass and increases risk of deployment success. It also poses difficulties in attitude control and requires a functioning power supply for the de-orbit duration. These points make the combined sail/tether concept unfavourable compared to a sail only satellite.

A sail only device with the sail segments angled (to form a cone shape) results in a design that has passive attitude stabilization.

8.1 Future work

Solar sails as a drag augmentation device have already been demonstrated by NanoSail-D and with upcoming missions such as CubeSail and LightSail-1 it can be argued that the technology readiness level for this application of solar sails is already at 7. The TRL needs to be advanced to 9 for the technology to become the primary form of satellite de-orbiting. Improvements to the current state of the technology would include proven deployment mechanisms, improved boom and sail materials, larger structures and attitude control advances.

Solar sailing has been demonstrated (by IKAROS from JAXA) but solar sailing missions in Earth orbit also require some advancement in terms of orbit analysis, attitude control and sail construction. One particular area of orbit analysis that requires attention is collision analysis, taking sail failure modes into account.

A deployable sail payload that can be fitted onto new satellites to satisfy IADC and UN guidelines is currently easily achievable, but using a deployable sail for ADR as proposed in this study is at a lower TRL. Docking onto debris pieces is a complex problem that requires more studying and demonstrators to advance the technology. The docking problem is present in almost every ADR solution – the exception being contactless alternatives.

The technology improvements and research effort that needs to be carried out to further the HybridSail concept described in this study is summarized in the table below.

Technology improvement	Priority	Complexity/effort
Advance TRL of deployable drag sail technology from 7 to 9	High	Medium
Advance TRL of solar sails in Earth orbit	High	Medium

Orbit analysis of solar sailing in Earth orbit (de-orbit manoeuvres using SRP)	High	Medium
Collision analysis, taking into account different object sizes and failure modes and tether collision probability	High	Medium
Attitude control of drag sails and solar sails	High	Medium
Advance TRL of debris docking solution	High	High
Advance TRL of tether construction and deployment	Low	High

9 References

1. H. Klinkrad, Collision Risk Analysis for Low Earth Orbit, Advance Space Research, Vol. 13, No. 8, 1993, pp. 177-186
2. H. Klinkrad, Space Object Catalogs, SSA Conference 15 Sep 2006, Colorado Springs
3. www.spacenewsfeed.co.uk, More Than 1,200 Satellites To Be Launched Over The Next 10 Years (summary of forecast by Euroconsult). Page accessed: 10 Feb 2011
4. J.-C. Liou, Collision activities in the future orbital debris environment, Advances in Space Research, Volume 38, Issue 9, 2006, Pages 2102-2106
5. J.-C. Liou, The Top 10 Questions for ADR, European Workshop on ADR, Paris 2010
6. INTER-AGENCY SPACE DEBRIS COORDINATION COMMITTEE, IADC Space Debris Mitigation Guidelines, IADC-02-01, September 2007
7. Battin, R. H., An Introduction to the Mathematics and Methods of Astrodynamics, American Institute of Aeronautics & Astronautics; Revised edition, 30 Jun 1999, ISBN 978-1563473425
8. D.A. Danielson, C.P. Sagovac, B. Neta and L.W. Early, Semi-analytic Satellite Theory, Naval Postgraduate School, Monterey, California, 1994
9. Department of Defence World Geodetic System 1984, NIMA TR8350.2 Technical Report
10. J. Meeus, Astronomical Algorithms, 2nd Edition, Willmann-Bell Inc., 1999
11. D.A. Vallado and D. Finkleman. A Critical Assessment of Satellite Drag and Atmospheric Density Modeling, AIAA/AAS Astrodynamics Specialist Conference in Honolulu HI, August 17-21, 2008. Paper no. AIAA-2008-6442.
12. M.L. Gargasz, Optimal spacecraft attitude control using aerodynamic torques, Thesis, Air Force Institute of Technology, AFIT/GA/ENY/07-M08, 2007
13. W.H. Steyn and V. Lappas, Cubesat Solar Sail 3-Axis Stabilization Using Active Sail Panel Translation and Magnetic Torquing, Aerospace Science and Technology, Article in press, doi:10.1016/j.ast.2010.09.009
14. K.O. Niehuss, H.C. Euler and W.W. Vaughan, Statistical technique for intermediate and long-range estimation of 13 month smoothed solar flux and geomagnetic index, NASA technical memorandum 4759, 1996
15. M.L. Cosmo and E.C. Lorenzini (editors), Tethers In Space Handbook, Smithsonian Astrophysical Observatory, 3rd Edition, 1997
16. P. Janhunen, Electrostatic Plasma Brake for Deorbiting a Satellite, Journal of Propulsion and Power, Vol. 26, No. 2, March-April 2010.
17. B. Wie, Solar Sail Attitude Control and Dynamics, Part I, Journal of Guidance, Control, and Dynamics, Vol. 27, No. 4, 2004, pp. 526-535.
18. C.R. McInnes, Solar Sailing: Technology, Dynamics and Mission Applications, 1st ed., Springer 2004

19. F.R. Hoots and R.L. Roehrich, SPACETRACK Report No. 3: Models for Propagation of NORAD Element Sets, Peterson AFB: Project Spacetrack Reports, Office of Astrodynamics, Aerospace Defense Center, 1988
20. L.G. Jacchia and J. Slowey, The Shape and Location of the Diurnal Bulge in the Upper Atmosphere, Smithsonian Astrophysical Observatory , SAO Special Report #207, 1966
21. H. Kinkrad, Collision risk analysis for low earth orbits, Advances in Space Research, Volume 13, Issue 8, August 1993, Pages 177-186
22. J.-C. Liou, Collision activities in the future orbital debris environment, Advances in Space Research, Volume 38, Issue 9, 2006, Pages 2102-2106
23. F. Martel, P.K. Pal and M. Psiaki, Active Magnetic Control System for Gravity Gradient Stabilized Spacecraft, Proceedings of the 2nd Annual AIAA/USU Conference on Small Satellites, Utah State University, September 1988.
24. W.T. Thomson, Spin Stabilization of Attitude against Gravity Torque, Journal of Astronautical Science, No.9, pp.31-33, 1962.
25. Harkness P, An aerostable drag-sail device for the deorbit and disposal of sub-tonne low Earth orbit spacecraft, PhD Thesis, Cranfield Universisty, 2006
26. R. Hoyt and R.L. Forward, Alternate interconnection Hoytether failure resistant multiline tether, U.S. Pat. 6286788 B1, 2001
27. SPECS, INC., Final Design of a Space Debris System, RFP #ASE274L,1990
28. EADS Astrium, http://www.esa.int/TEC/Robotics/SEMTWLKKKSE_0.html, page last accessed: 7 June 2011.
29. Beihang University, Presentation, 1st IAA Conference on University Satellites Missions and Cubesat Workshop, Rome, Italy,2002
30. QinetiQ, Robotic Geostationary orbit Restorer (ROGER) Executive Summary, ESA/ESTEC Contract No. 15678/01/NL/WK,2003
31. S. Nishida, T. Yoshikawa, A Robotic Small Satellite for Space Debris Capture, Proceedings of the 2008 IEEE International Conference on Robotics and Biomimetics Bangkok, Thailand, February 21 - 26, 2009
32. S. Nishida et al., Space debris removal system using a small satellite, Acta Astronautica 65 (2009) 95–102
33. S. Hobbs, Debris Removal from Low Earth Orbit DR LEO, College of Aeronautics Report 1001, ISBN 978-1-907413-04-9, 2010
34. R. Hoyt, Space Debris Mitigation Technologies, Tethers Unlimited, Inc
35. C. McInnes, Solar Sailing: Technology, Dynamics and Mission Applications, Praxis Publishing Ltd, Chichester, UK, 1999, pp. 19 – 24.
36. Macdonald, M, Hughes, GW, McInnes, C, Lyngvi, A, Falkner, P and Atzei, A (2007) GeoSail: An elegant solar sail demonstration mission. Journal of Spacecraft and Rockets, 44 . pp. 784-796.
37. Fekete, T.A., Sackett, L. L., von Flotow, A.H., Trajectory Design for Solar Sailing from LowEarth Orbit to the Moon, AAS 92-184, Advances in Astronautical Sciences, Vol. 79, Pt. 3, pp. 1083-1094, 1992
38. Sands, N., Escape from Planetary Gravitational Fields by Using Solar Sails, American Rocket Society Journal, Vol. 31, pp. 527-531, April 1961

39. Sauer, Jr., C.G., Optimal Solar Sail Interplanetary Trajectories, American Institute of Aeronautics and Astronautics and American Astronautical Society, Astrodynamics Conference, San Diego, Calif., Aug. 18-20, 1976
40. Macdonald M., McInnes C. R., Analytical Control Laws for Planet-Centred Solar Sailing, Journal of Guidance, Control, and Dynamics, Vol. 28, No. 5, pp. 1038-1048, 2005
41. Sackett, L.L. & Edelbaum, T.N., Optimal Solar Sail Spiral to Escape, Advances in Astronautical Sciences, AAS/AIAA Astrodynamics Conference, A78 31-901, 1978